UCLouvain

École polytechnique de Louvain

Twisted 2D-Materials: CrSBr

Author: **Louis Smet**
Supervisor 1: **Prof. P. Gehring**
Supervisor 2: **A. Canetta**
Readers: **Prof. B. Hackens**
Academic year 2023-2024
Specialised Master in Nanotechnologies

Abstract

This dissertation explores the properties, theoretical calculations, fabrication techniques, and characterization of two-dimensional (2D) materials, with a particular focus on CrSBr (chromium sulfide bromide) and its twisted heterostructures. The research is motivated by the growing interest in 2D materials for their unique electronic, optical, and mechanical properties, which make them suitable for a wide range of applications in nanotechnology and materials science. The first section provides an extensive introduction to 2D materials, tracing their history and highlighting the significance of CrSBr, a lesser-known yet promising member of this class. Including an introduction to twisted heterostructures, which have emergence of novel phenomena such as Moiré superlattices. The second section presents theoretical calculations aimed at evaluating the refractive index of CrSBr using first-principles methods, such as Density Functional Theory (DFT). These calculations provide insights into the electronic and optical properties of CrSBr, which are critical for potential applications in optoelectronics and spintronics. The third section details the fabrication techniques used to produce high-quality monolayers and twisted heterostructures of CrSBr. Followed by the characterization of these fabricated materials in the fourth section. The Piezoresponse Force Microscopy (PFM) method is described, followed by its application to both twisted bilayer graphene and twisted CrSBr. The work concludes by summarizing the findings and discussing the implications for future research.

Preface

I am thankful for the great experience I had doing my master thesis at the Functional Quantum Devices Group of Prof. Pascal Gehring. I got to experience many different aspects of performing experimental research, which were previously unknown to me. For instance, working in a modern clean room environment. Because of this excellent experience, I look at performing research much more positively. For this, I am very thankful. Next, I want to thank my supervisor Alessandra Canetta for guiding me during this journey. It is near certain that any good part of this work, would not have been possible without her. I am extremely thankful that she was my supervisor. I want to also thank Pascal for always pushing possibilities to the limits. He really makes you question how far one can go and he encourages you to try to go as far as possible. Lastly, I want to especially thank the entire group for being so patient with me. It is unfortunate that I wasn't able to hand in this work earlier due to personal reasons, but I am happy with result nevertheless.

Contents

1 Introduction on 2D Materials

> *My life has become much easier since I've learned to say "no" to Pascal.*
>
> — **Valentin Fonck**
> (Ph.D. student of Prof. Gehring.)

Two-dimensional (2D) materials, characterized by their atomic-scale thickness, possess unique physical, chemical, and electronic properties distinct from their bulk counterparts. These materials, often described as having one dimension confined to the nanoscale, typically consist of a single or a few layers of atoms. Their structure imparts properties that are highly anisotropic, leading to novel applications and phenomena that are not achievable with traditional three-dimensional materials.

The study of 2D materials spans multiple disciplines, including physics, chemistry, materials science, and engineering. Their potential applications range from next-generation electronic devices to energy storage systems, sensors, and even quantum computing. As the field continues to expand, understanding the fundamental properties and behavior of these materials has become a critical area of research.

1.1 History

The concept of 2D materials, while seemingly modern, has its roots in earlier theoretical work. Before the isolation of graphene, the existence of single-layer crystals was largely considered hypothetical due to the presumed instability of such structures. However, the success in exfoliating graphene from graphite using simple mechanical cleavage techniques dispelled these notions and demonstrated that 2D materials could exist in stable forms.

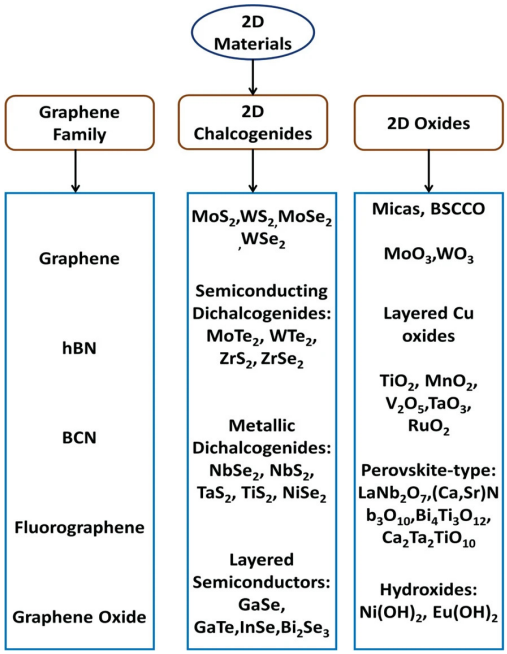

Fig. 1.1.: The family of 2D materials. Figure taken from [9].

The discovery of graphene in 2004 by Geim and Novoselov [26] marked the dawn of a new era in materials science, catalyzing the exploration and development of 2D materials. Graphene, a single layer of carbon atoms arranged in a hexagonal lattice, exhibited remarkable properties such as exceptional electrical conductivity [38], mechanical strength [29], and thermal conductivity [38]. This groundbreaking work earned the researchers the Nobel Prize in Physics in 2010 and started numerous investigations of a vast family of 2D materials.

Following graphene, researchers quickly turned their attention to other layered materials, particularly those belonging to the transition metal dichalcogenides (TMDs), hexagonal boron nitride (h-BN), and other compounds. (See Figure 1.1) The realization that many bulk materials could be reduced to atomically thin layers without losing structural integrity or functionality, sparked a renaissance in the study of these materials.

Presently, the theoretically recognized number of stable 2D materials is around 700. [32] Although some of them are yet to be synthesized. Because of these exquisite properties found in graphene compared to its 3D counterpart, lots of new research is being done (as shown in Figure 1.2) on different 2D materials in various contexts.

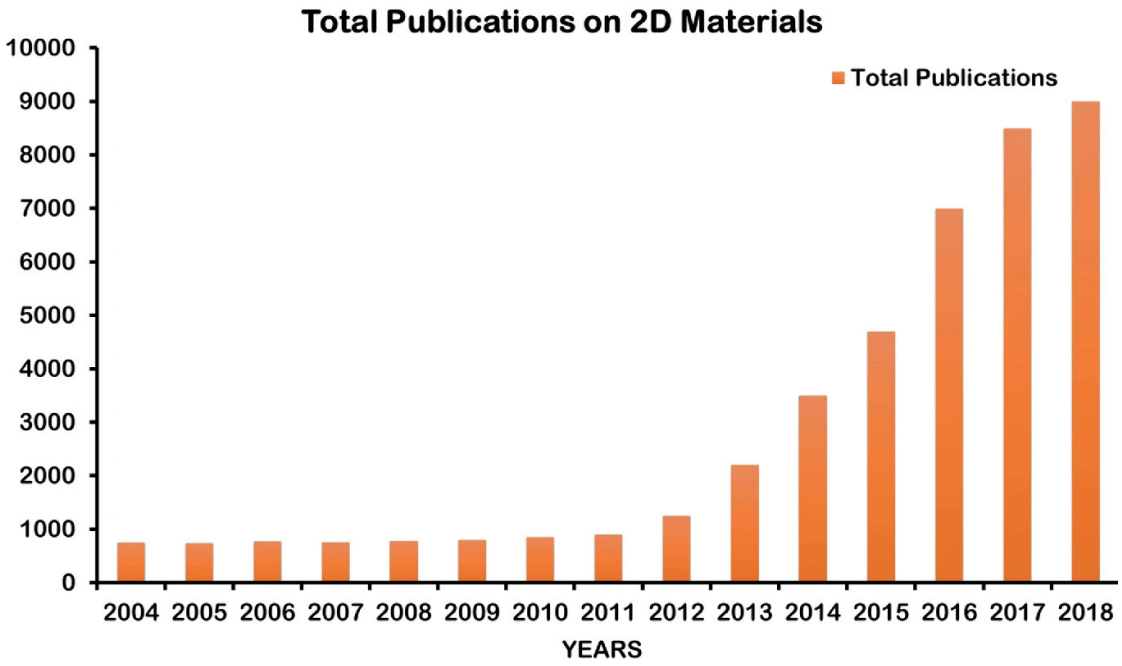

Fig. 1.2.: Increasing trend of the total 2D material publications per year. Figure taken from [9].

1.2 CrSBr

One of the latest 2D material to attract the attention of the scientific community is Chromium Sulfide Bromide (CrSBr), shown in Figure 1.3. CrSBr is composed by two fused buckled planes of CrS, sandwiched between Br atoms and stacked along the c axis, and crystallizes in the orthorhombic Pmmn space group. As can be seen from Figure 1.4, it is a layered van der Waals (vdW) material. That is, just like graphite, a layering of 2D sheets held together by vdW forces.

Although there are no covalent bonds between layers, there are magnetic interlayer interactions. The magnetically active chromium atoms (red arrows) interact ferromagnetically (FM) intralayer and anti-ferromagnetically (AFM) interlayer for $T < T_N$. The Néel temperature $T_N = 132$ K, well above the boiling point of liquid nitrogen, is one of the highest among 2D antiferromagnets [13]. DFT-calculations show that the intralayer interaction $J_{\parallel} = -13$ meV is an order of magnitude larger than interlayer interaction $J_{\perp} = 1.5$ meV. [18]

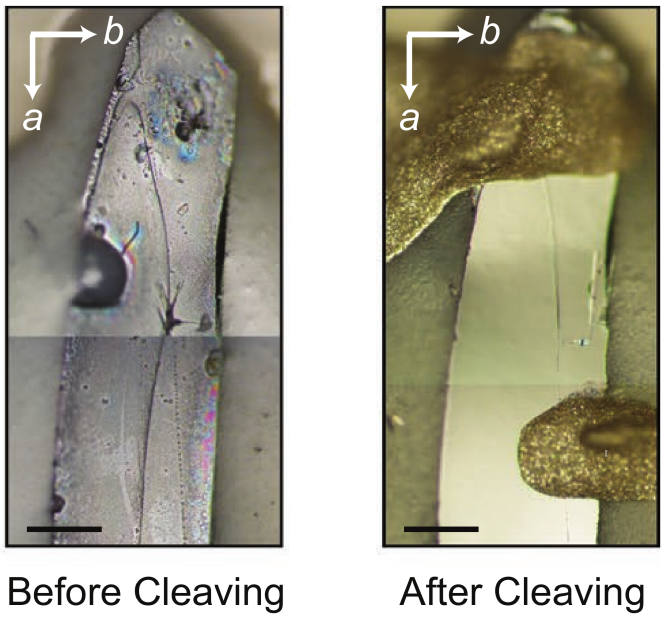

Fig. 1.3.: Optical images of a CrSBr single crystal before (left) and after (right) mechanically cleaving with Scotch tape. The scale bars are $100\ \mu$m. Orientation of the crystal axes are given in the inset. Figure taken from [40].

On top of that, it is a semiconductor with a band gap of $1.5 - 2$ eV [41]. Semiconductors have tunable electronic properties, on the other hand magnets have tunable spin configurations. In CrSBr, both of these properties are therefore present and is classified as a magnetic semiconductor. That makes CrSBr very attractive for potential spintronic applications.

However, in spite of the recently performed research into the transport and magnetic properties of this material, there are still many other features that have not been investigated yet. Among them, the refractive index of CrSBr has not been reported to date. Considering the difficulty in optically assessing if a flake of a 2D material is in fact monolayer, optimising the conditions to do so is therefore very useful. To this end, the following chapters will contain theoretical calculations of the refractive index. Subsequently this obtained refractive index will be used to calculate ideal conditions for optimal identification of monolayers in different fabrication and or transfer techniques.

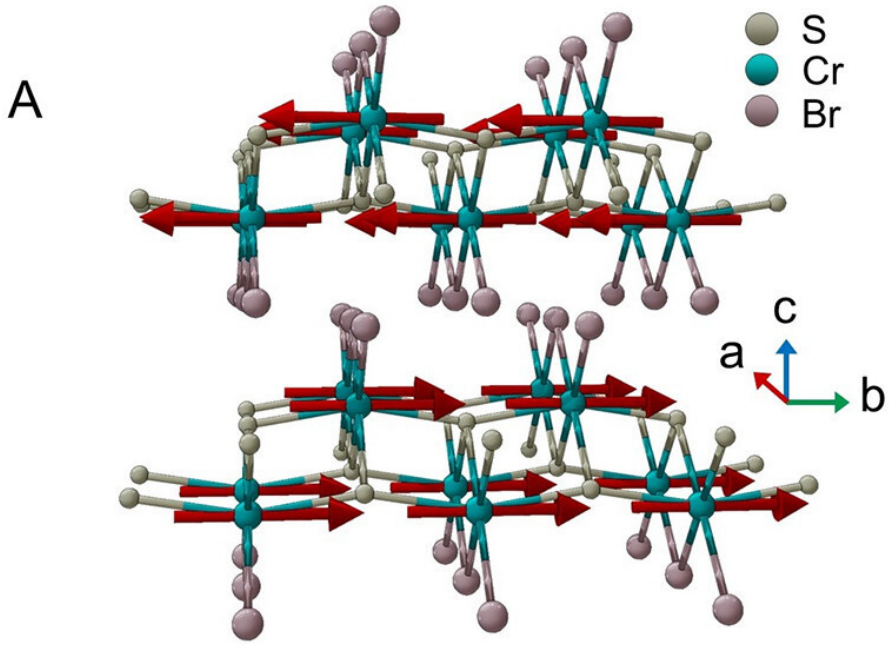

Fig. 1.4.: Crystal structure of the layered magnetic semiconductor CrSBr. Red arrows indicate the spin direction of the Cr atoms. Figure taken from [22].

1.3 Monolayer

Quantum mechanics has taught us that confining a system in one dimension gives rise to new physics. This is precisely what happens when the monolayer limit is reached for a vdW material. Many TMDs become direct band gap semiconductors in the monolayer, even though their bulk counterpart is an indirect band gap semiconductor. This is shown in Figure 1.5 for MoS_2, but is true for many TMDs. In the monolayer limit, TMDs therefore become easily excitable via light and that makes them ideal for optoelectronic purposes. In the case of CrSBr, in the monolayer limit it becomes a ferromagnetic material and the band gap also becomes direct, as will be discussed in chapter 2.

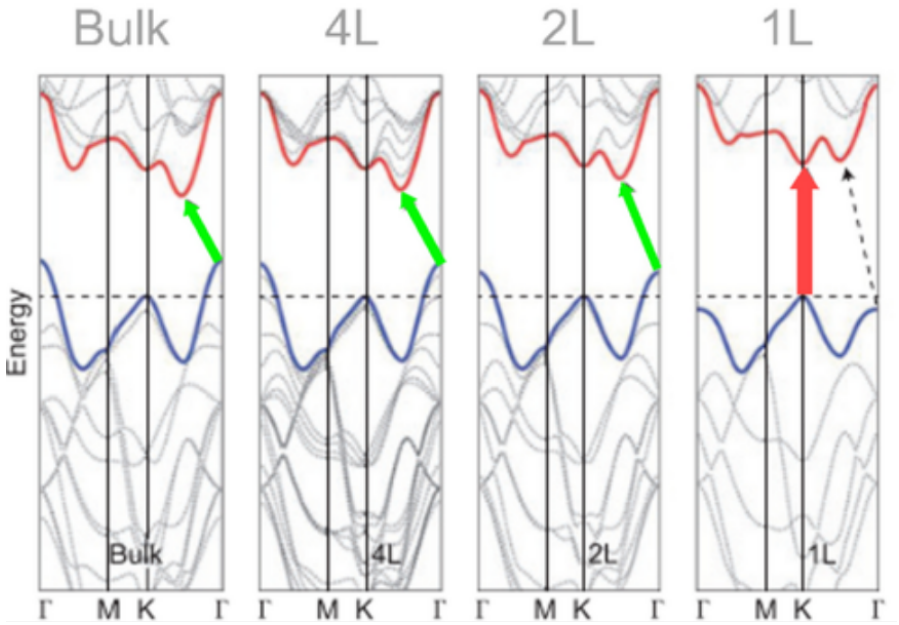

Fig. 1.5.: Layer dependent bandstructure for MoS_2. Figure taken from [21].

1.4 Twisted heterostructures

Twisted heterostructures, also known as Moiré superlattices, represent a frontier in the field of condensed matter physics and materials science. These structures arise when two or more layers of 2D materials are stacked with a relative twist angle between them, leading to the formation of new periodic patterns and emergent properties that are not present in the individual layers. The discovery of novel phenomena in these twisted heterostructures, such as superconductivity in twisted bilayer graphene [7], has opened up new avenues for research and applications in areas including electronics, optoelectronics, quantum computing, and materials engineering. [20]

The concept of twisting layered materials to tune their properties is rooted in the quantum mechanical interactions that arise from the periodic potential of the Moiré pattern. This pattern is created when the atomic lattices of the two layers are misaligned by a small angle, resulting in a superlattice with a periodicity much larger than that of the original atomic lattices, as shown in Figure 1.6. The Moiré superlattice can profoundly alter the

electronic, optical, and mechanical properties of the heterostructure, giving rise to a rich spectrum of new physical phenomena.

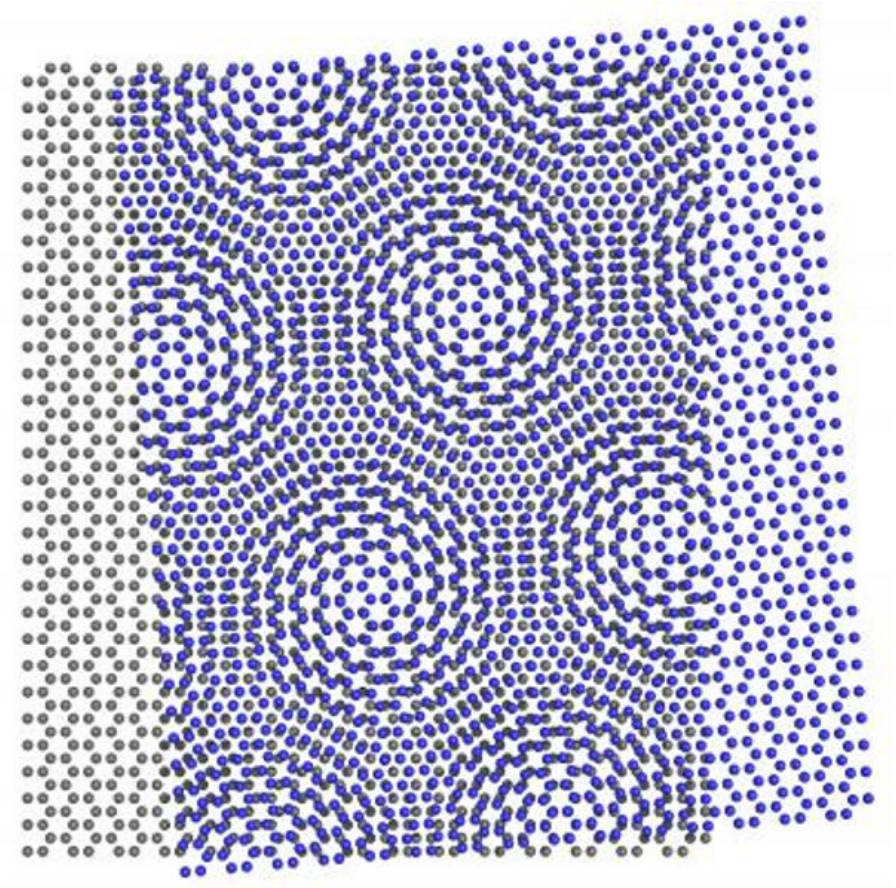

Fig. 1.6.: Moiré pattern of 2 graphene sheets twisted relative to each other. Figure taken from [25].

The idea of twisting layers to create Moiré patterns, gained significant attention after the discovery of superconductivity in twisted bilayer graphene at the so-called "magic angle" ($\sim 1.1°$) by Cao, Y. et al. in 2018. [7] This discovery revealed that a small twist could drastically alter the electronic properties of the material, leading to phenomena such as correlated insulating states and unconventional superconductivity. This groundbreaking work sparked a surge of interest in twisted heterostructures, extending the concept to other 2D materials and complex multi-layered systems. The goal of this work will therefore be to obtain such twisted heterostructure with the not fully explored material CrSBr.

2 Theoretical Calculations

> *Life is cruel. Why should the afterlife be any different?*
>
> **— Davy Jones**
> (Pirates of the Caribbean)

Although intense research about the transport and magnetic properties of CrSBr have recently been performed [41], there are still many other features that have not been investigated yet. Among them, the refractive index of CrSBr has not been experimentally evaluated to date. Additionally, the few numerical works reporting the optical properties of this material do not mention the aforementioned parameter. Knowing the refractive index is extremely useful in the field of 2D materials, as it helps assessing the thickness of the flakes by simple optical identification, and therefore allows to optimise the fabrication process. For these reasons, the first part of this work consists in the theoretical evaluation of the refractive index of the CrSBr.

2.1 Evaluation of the band structure of CrSBr

The open-source package ABINIT is used to perform the calculations. [1] Before going straight into the refractive index calculations, an intermediate goal is set first to obtain the material's band structure. This can then be compared with other computations performed in the literature. An example of a band structure from the literature is shown in Figure 2.1.

The electronic structure depends on the atomic positions and lattice parameters, and therefore needs either to be taken from an experiment or to be determined from theory. On top of this, the potential for the Schrodinger equation also relies on numerically well-controlled parameters such as ecut and kpoints. To this end, convergence studies of

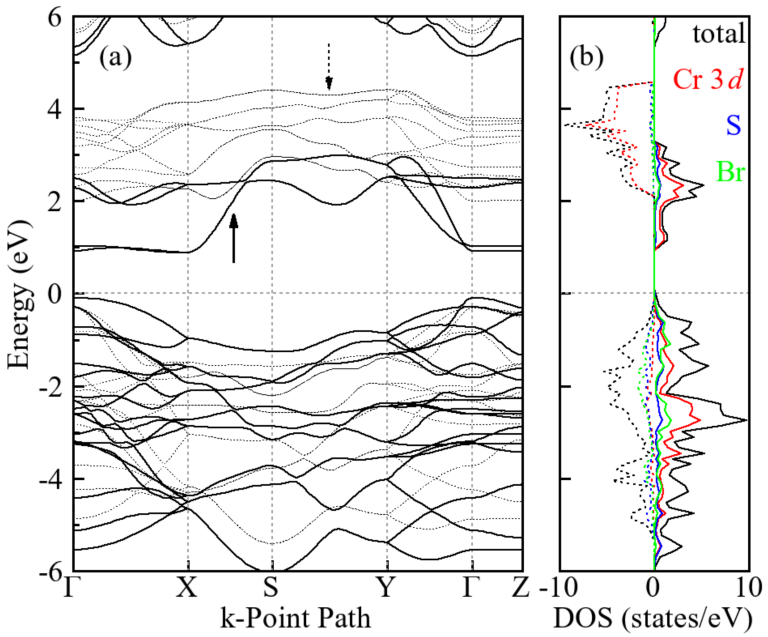

Fig. 2.1.: **a)** The band structure of CrSBr bulk is calculated by GGA+U. The solid (dashed) lines represent the up (down) spin. The Fermi level is set at zero energy. **b)** Density of states (DOS): the black curves represent the total DOS, and the red, blue, and green curves refer to the Cr 3d, S, and Br contributions, respectively. Figure taken from [46].

the total energy with respect to the ecut value and with respect to the kpoints were performed. After this, a relaxation of the lattice parameters is performed again with respect to both the ecut value and the kpoints. Relative convergence studies are performed, and the total energy value shall be considered converged once the accuracy lies within 0.5 mHartree per atom.

Concretely, an interval with a width of $0.5 \cdot 6 = 3$ mHartree is plotted centered around the total energy value corresponding to the most stringent ecut or kpoint value. Analogously a dependent (ex. a lattice parameter) is considered converged once the accuracy lays within 0.2%. Concretely, an interval is plotted centered around the dependent value that corresponds with the most stringent variable value (ex. ecut) with a width of $0.002 \cdot$ most-stringent-dependent-value. Once multiple values lay within the interval, the parameter under consideration is considered converged. Unless otherwise stated, the least stringent value within the interval will be shown in the caption and used for further convergence studies.

2.1.1 Preliminary calculations

Firstly, an attempt is made with the simplest formalism, a DFT calculation with norm-conserving LDA potentials [34]. No spin polarisation nor van der Waals correction is applied. The obtained band structure is completely off when compared with the literature. The branches of neither the conduction band nor the valence band are similar. Nevertheless, more importantly, there was no band gap. This explains why the convergence studies took a considerable amount of time. From the perspective of the DFT framework, the material was metal-like and therefore required to be treated as a metal under this framework (via tsmear). This behaviour may occur because DFT cannot correctly assess the localisation nature of the d-electrons of the chromium atoms. However, the material is not a metal but a semiconductor with a small band gap; thus, treating it like a metal is not the solution. Therefore, more advanced schemes shall be adopted to overcome this.

2.1.2 Projector Augmented-Wave (PAW)

Based on these preliminary results, some adjustments shall be made to improve the result. From now on, the spin of the atoms will be included by performing spin-polarised calculations. This additional degree of freedom is necessary to more accurately describe the material. Additionally, due to the unique character of the material, as discussed in section 1.2, the material is ferromagnetic in-plane and anti-ferromagnetic out-of-plane. To circumvent the problem of modelling this behaviour, a monolayer of CrSBr shall be considered from this moment onward. This solves several minor issues. Foremost, as discussed in sec. 1.3, monolayers have desirable properties. Secondly, there is no longer a need for van der Waals corrections in the calculations. Then, last and most importantly, beside the amelioration of the computational load, this choice also allows to ignore the vdW interactions, as well as directly consider the ferromagnetic order only. On the other hand, the study of a monolayer requires an additional vacuum slab convergence study. Such added difficulty is however compensated by the aforementioned benefits.

In addition, the scheme shall also be changed to the so-called DFT+U scheme later. This is the same scheme that produced Figure 2.1. To implement this, it was necessary to switch to PAW potentials (PBE) [36]. To prevent the same mistake from happening as in section 2.1.1, the band structure was first calculated to see if a band gap was formed.

This was done using values obtained from previous calculations and suggested values from the literature. Therefore, the result is just an approximation, however it represents a first reference from which more accurate data can be calculated. After it is found, proper convergence studies are done. First, with $U = 0$ eV and $J = 0$ eV (DFT), using the obtained values, a search was performed for the optimal U and J value, and then another convergence study was performed with that specific U and J (DFT+U). During DFT+U calculations, the ABINIT value usepawu 1 was used.

Preliminary band structure

With the adjustments and using the values ecut $= 17.5$ and pawecutdg $= 35$, kpoints $= [8$ 8 $1]$, $c = 14.96$ Å and $U = 0$ eV, $J = 0$ eV the band structure is calculated. From now on, pawecutdg shall no longer be reported but will always be chosen pawecutdg $=$ ecut $\cdot\, 2$. The result is shown in Figure 2.2.

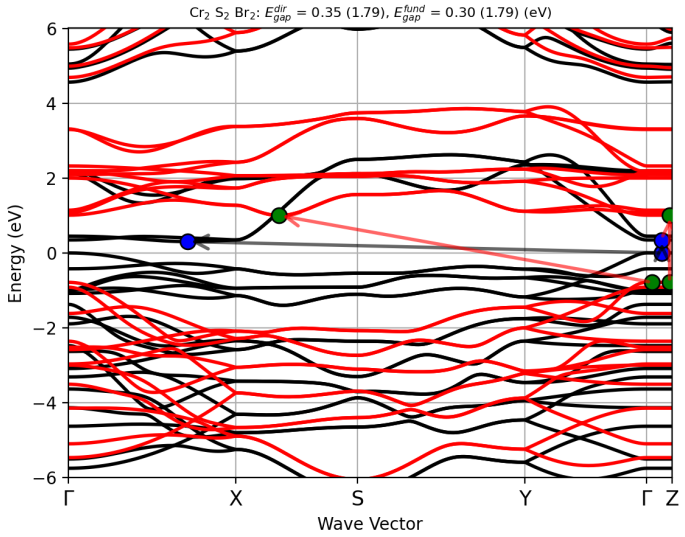

Fig. 2.2.: Preliminary obtained band structure of monolayer CrSBr in DFT, $U = 0$ eV and $J = 0$ eV. The black (red) lines represent the up (down) spin electron bandstructure and there respective band gap transitions in blue (green).

Despite the band gap value still not being correct, the DFT calculations with spin polarisation correctly interpret the material as a semiconductor. Consequently, it is possible to

proceed with formal convergence studies, which are reported here below.

Vacuum

First, the convergence study with respect to the vacuum is done with ecut $= 17.5$ and kpoints $= [8\ 8\ 1]$. The unit cell of bulk CrSBr has a c-axis length of 7.96 Å. The convergence starts there and gradually increases.

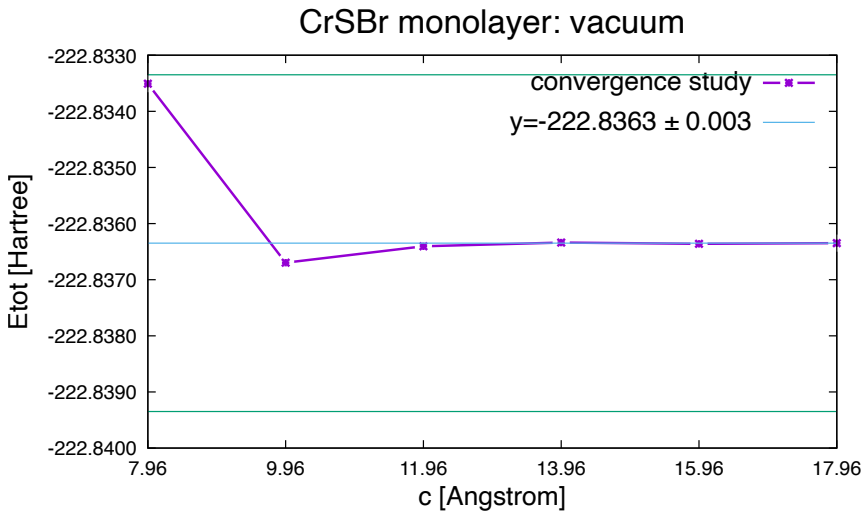

Fig. 2.3.: Convergence study of total energy with respect to the c-axis for monolayer CrSBr in DFT, $U = 0$ eV and $J = 0$ eV. Obtained value c $= 7.96$ Å.

A conservative value of $c = 13.96$ Å was taken instead of the value $c = 7.96$ Å put forward by the convergence study, which corresponds with the bulk case. This was done to ensure no interactions occurred because multiple literature studies reported using $c = 15$ Å or more. [46, 4, 45]

Total energy: U=0, J=0

The convergence studies of the total energy with respect to both ecut and kpoints are shown in Figure 2.4 and Figure 2.5, respectively. Because the SCF cycle had more trouble

converging with kpoints $= [4\ 4\ 1]$ it was opted to take kpoints $= [8\ 8\ 1]$ instead.

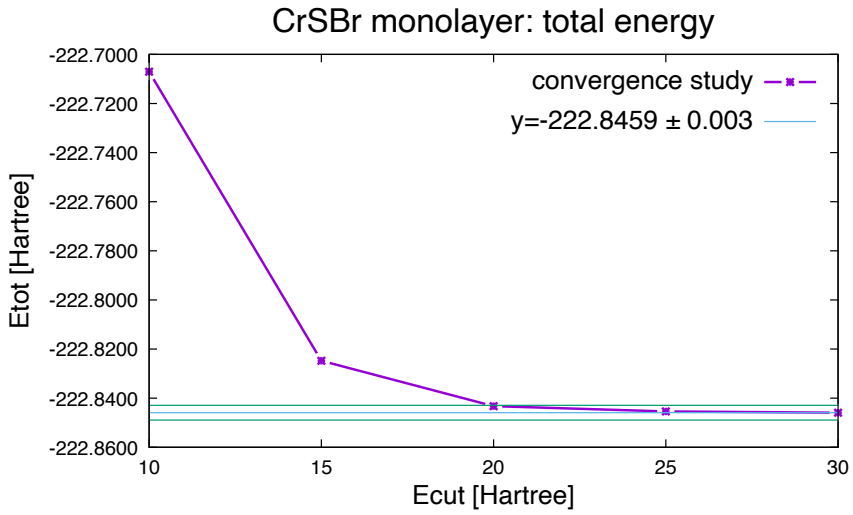

Fig. 2.4.: Convergence study of total energy with respect to ecut for monolayer CrSBr in DFT, $U = 0$ eV and $J = 0$ eV. Obtained value ecut $= 20$.

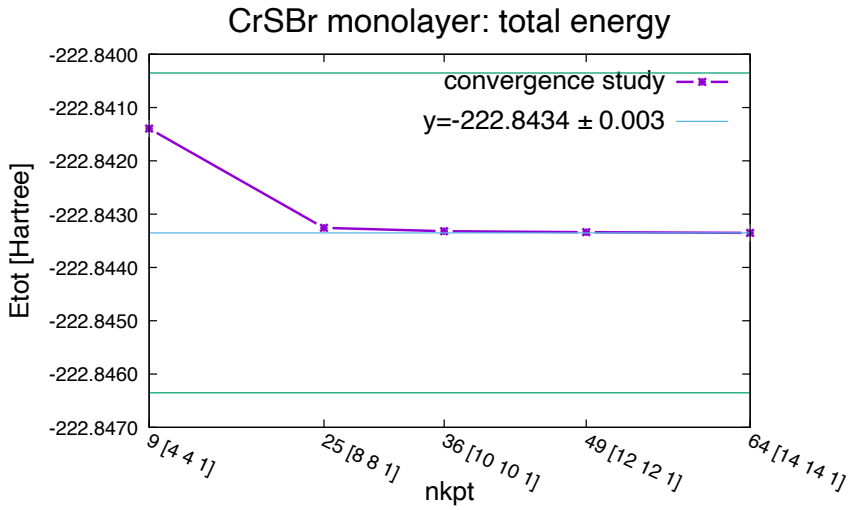

Fig. 2.5.: Convergence study of total energy with respect to kpoints for monolayer CrSBr in DFT, $U = 0$ eV and $J = 0$ eV. Obtained value kpoints $= [4\ 4\ 1]$.

Relaxation: U=0, J=0

Because a monolayer is considered, the c-axis is not allowed to relax. Only data for the a- and b-axis is available. The results are shown in Figure 2.6 and Figure 2.7, respectively.

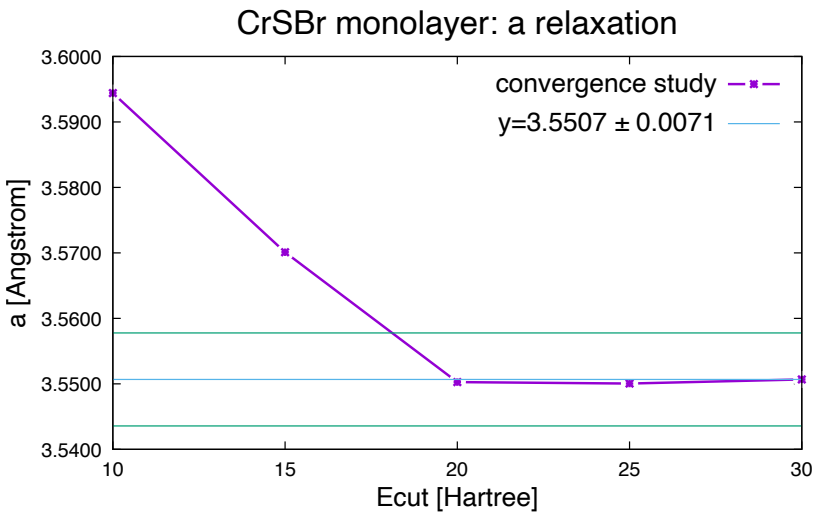

Fig. 2.6.: Convergence study of a-axis with respect to ecut for monolayer CrSBr in DFT, $U = 0$ eV and $J = 0$ eV. Obtained value ecut $= 20$.

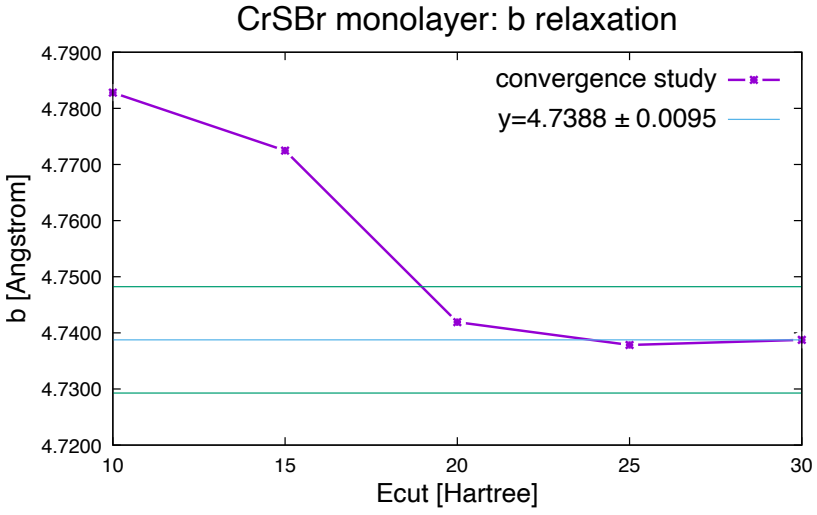

Fig. 2.7.: Convergence study of b-axis with respect to ecut for monolayer CrSBr in DFT, $U = 0$ eV and $J = 0$ eV. Obtained value ecut $= 20$.

Next, a relaxation of the lattice parameters with respect to the kpoints is considered. The results are shown in Figure 2.8 and Figure 2.9, respectively.

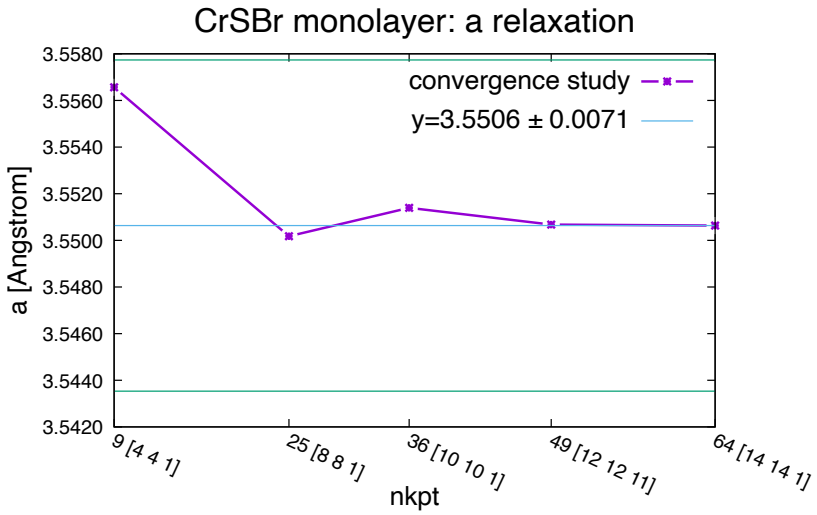

Fig. 2.8.: Convergence study of a-axis with respect to kpoints for monolayer CrSBr in DFT, $U = 0$ eV and $J = 0$ eV. Obtained value kpoints $= [4\ 4\ 1]$.

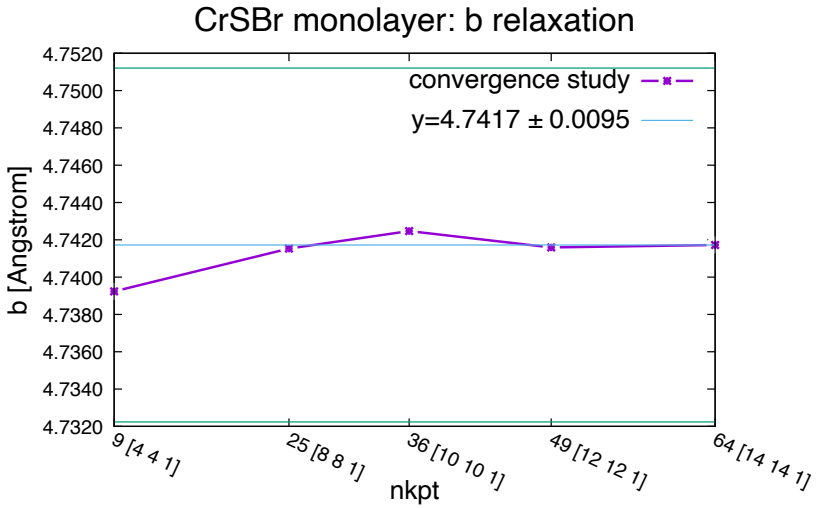

Fig. 2.9.: Convergence study of b-axis with respect to kpoints for monolayer CrSBr in DFT, $U = 0$ eV and $J = 0$ eV. Obtained value kpoints $= [4\ 4\ 1]$.

Given the convergence studies and the aforementioned remarks, the values ecut $= 20$, kpoints $= [8\ 8\ 1]$, and $c = 13.96$ Å shall be used to continue. The obtained results for the

lattice parameters are also in line with the experimentally found values of $a = 3.50$ Å, $b = 4.76$ Å, $c = 7.96$ Å. [39]

Band structure: U=0, J=0 The band structure obtained by applying the properly obtained values for ecut and kpoints is shown in Figure 2.10.

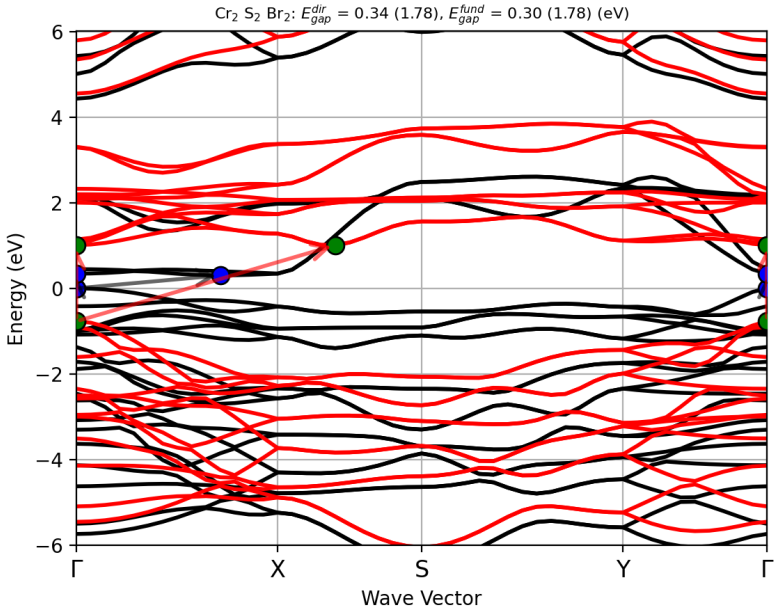

Fig. 2.10.: Obtained band structure of monolayer CrSBr in DFT, $U = 0$ eV and $J = 0$ eV. The black (red) lines represent the up (down) spin electron bandstructure and there respective band gap transitions in blue (green).

Even though a band gap is still present, its value results smaller compared to the experimental value of $\Delta_E = 1.5 \pm 0.2$ eV. [39] Note that the band structure has changed with respect to Figure 2.2. This clearly shows the necessity of performing convergence studies.

Band structure: U=6, J=0.8

The newly obtained values were used as a starting point to open the band gap further; for multiple combinations of U and J, the band structure was calculated, and the resulting

band gap was compared with the experimental value. In Yang et al., 2021 the values $U = 4$ and $J = 0.8$ eV were taken. [46] This gives us a rough estimate to probe around. In the end, the value $U = 6$ eV and $J = 0.8$ eV was used, resulting in the band structure in Figure 2.11. This choice for $U = 6$ eV and $J = 0.8$ eV was based upon how well the band gap in the calculated band structure that results from these values corresponds with the experimentally found value and other literature studies. More accurate approaches can be used to perform this evaluation, however this goes beyond the scope of this thesis. The band structure from the literature is shown in Figure 2.12

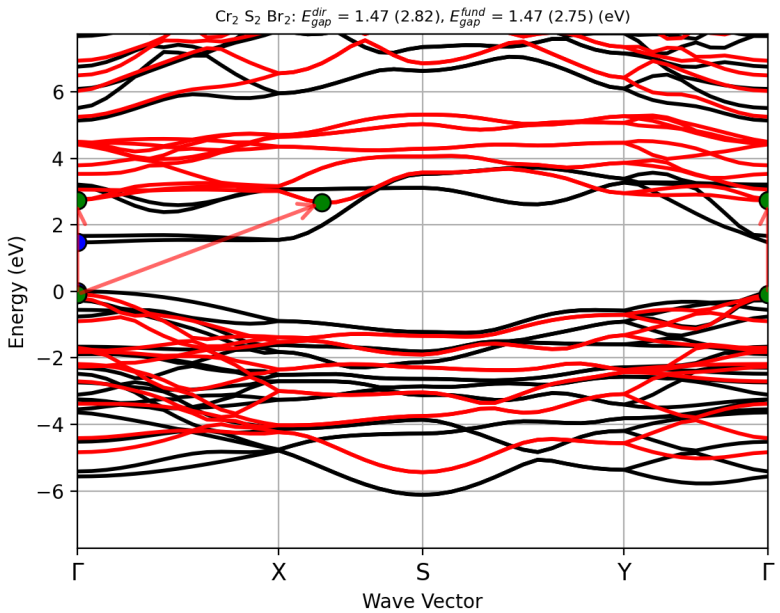

Fig. 2.11.: Obtained band structure of monolayer CrSBr in DFT+U, $U = 6$ eV and $J = 0.8$ eV. The black (red) lines represent the up (down) spin electron bandstructure and there respective band gap transitions in blue (green).

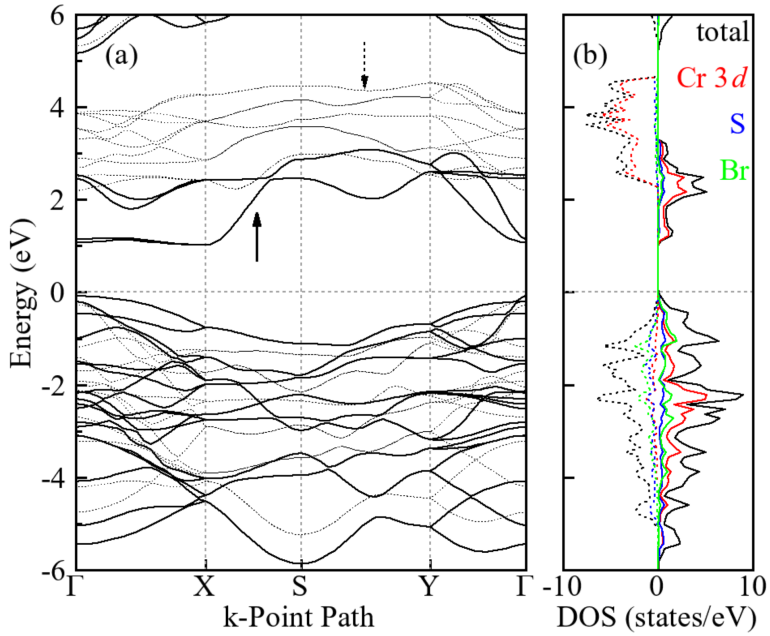

Fig. 2.12.: The band structure and DOS for CrSBr monolayer by GGA+U. See Figure 2.1 for a comparison. Figure taken from [46].

The band structure is now in excellent agreement with the literature, and the band gap complies with the experimental value. It is important to underline that the U not only makes the band gap larger but also impacts the bands themselves. For instance, in Figure 2.10, there is also an indirect band gap, whilst, in Figure 2.11, there is only a direct band gap. A new convergence study was done just as for the case $U = 0$ eV and $J = 0$ eV but with the new values for $U = 6$ eV and $J = 0.8$ eV. The results are available in the appendix section A.1.

2.2 Evaluation of the refractive index of CrSBr

Now that a correct band structure is obtained, an attempt can be made to calculate the dielectric tensor, and from that, the refractive index can be obtained. Different possible routes can be taken to calculate the refractive index. It was opted to pursue the density-functional perturbation theory (DFPT) route because the ABINIT documentation explicitly stated it is compatible with DFT+U: “Thanks to the locality provided by PAW partial wave basis, it is possible to perform response function calculations for correlated

electron materials. The DFT+U formalism is usable without any restriction for the PAW + DFPT calculations." [10] . However, due to important computational difficulties, it was also opted to start preliminary attempts in GW and optic in parallel. During this time, a breakthrough was made in the DFPT route, and the preliminary attempts were also diverging; it was opted to stop the additional routes.

The DFPT route calculates the dielectric tensor at zero frequency, and the resulting dielectric tensor is diagonal and has only real values. The refractive index in the x, y and z directions can be extracted if $\mu \approx 1$ is assumed. Even though this assumption might not be fully correct for a magnetically active material as CrSBr, it can still be considered acceptable as a first order approximation.

$$n_x \approx \sqrt{\epsilon_{11}}, \quad n_y \approx \sqrt{\epsilon_{22}}, \quad n_z \approx \sqrt{\epsilon_{33}} \tag{2.1}$$

The convergence study results of the DFPT calculations are presented hereafter.

2.2.1 DFT+U

First of all, because of stability reasons, a switch to PAW LDA potentials [35] was made. The choice for LDA is because it is considered more tested, and given diverging issues, stability seemed desirable. In theory, this can have an impact on earlier performed convergence studies, but this is considered negligible. Even though a convergence study with respect to the total energy and lattice parameters was already done previously, it is absolutely necessary to do one again for the refractive index of interest. This shall become clear in the results that follow. The obtained values of the old convergence studies (section A.1) were chosen as the starting values for the new convergence studies. Unfortunately, this resulted in diverging results with resulting values for the refractive index $n_x, n_y, n_z > 10000$. Therefore, finding suitable values to start a proper convergence study took some trial and error. One of the points in configuration space that worked was: ecut 30, ngkpt [14 14 1] and $c = 11.96$ Å. This point was chosen as the starting point for the convergence studies. If the obtained value from the convergence studies of individual directions disagrees, the most stringent value is chosen to proceed to the subsequent convergence study.

Ecut

The convergence studies of n_x, n_y and n_z with respect to ecut are shown in Figure 2.13, Figure 2.14 and Figure 2.15, respectively. Note that ecut $= 20$ diverged.

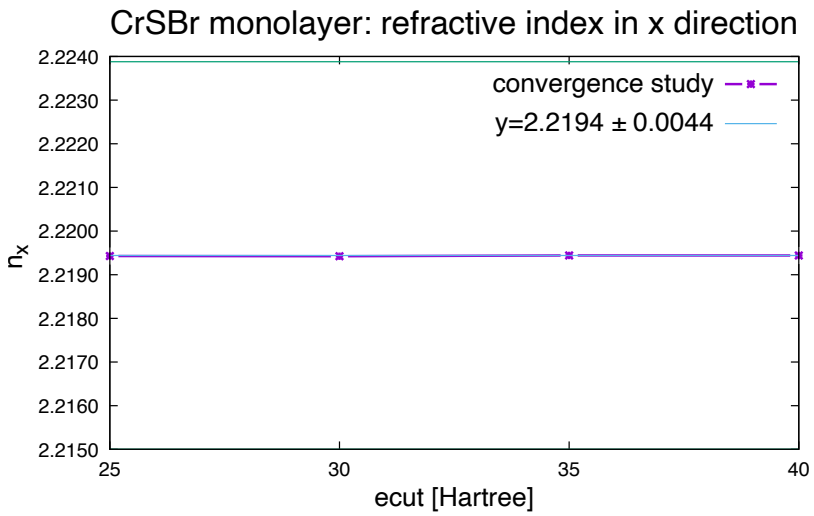

Fig. 2.13.: Convergence study of n_x with respect to ecut for monolayer CrSBr in DFT+U, $U = 6$ eV and $J = 0.8$ eV. Obtained value ecut $= 25$.

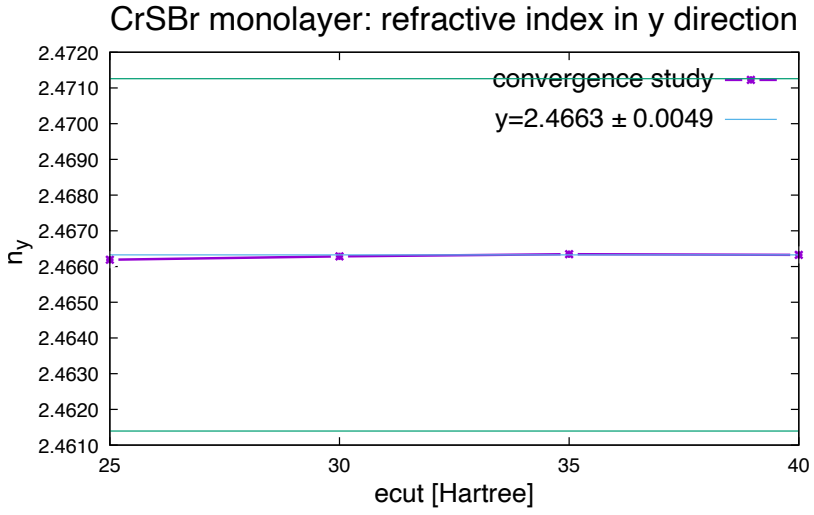

Fig. 2.14.: Convergence study of n_y with respect to ecut for monolayer CrSBr in DFT+U, $U = 6$ eV and $J = 0.8$ eV. Obtained value ecut $= 25$.

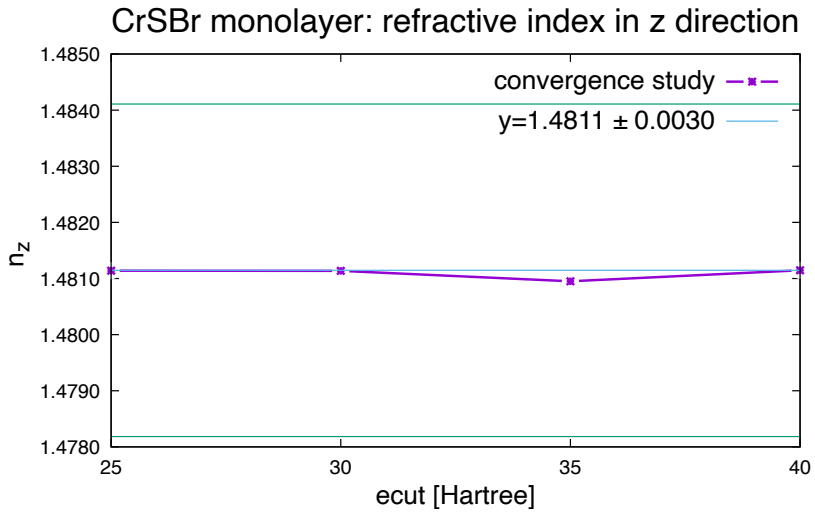

Fig. 2.15.: Convergence study of n_z with respect to ecut for monolayer CrSBr in DFT+U, $U = 6$ eV and $J = 0.8$ eV. Obtained value ecut $= 25$.

Kpoints

The convergence studies of n_x, n_y and n_z (ecut $= 25$) with respect to kpoints are shown in Figure 2.16, Figure 2.17 and Figure 2.18, respectively.

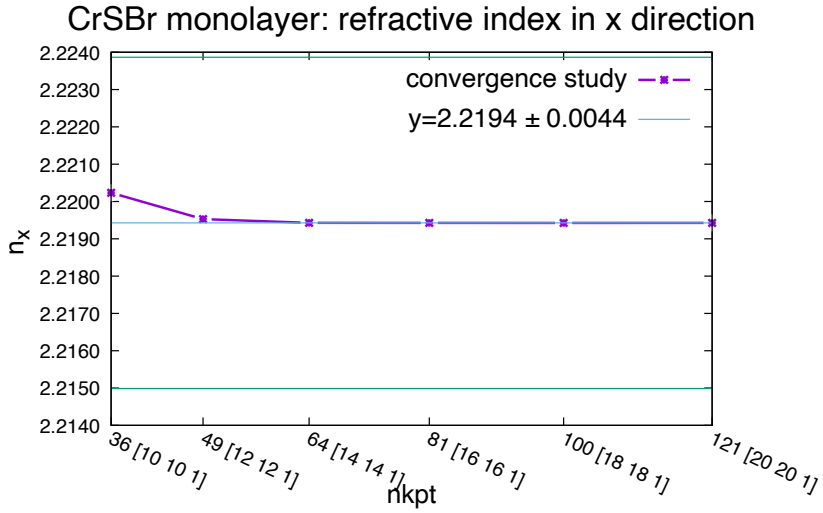

Fig. 2.16.: Convergence study of n_x with respect to kpoints for monolayer CrSBr in DFT+U, $U = 6$ eV and $J = 0.8$ eV. Obtained value kpoints $= [10\ 10\ 1]$.

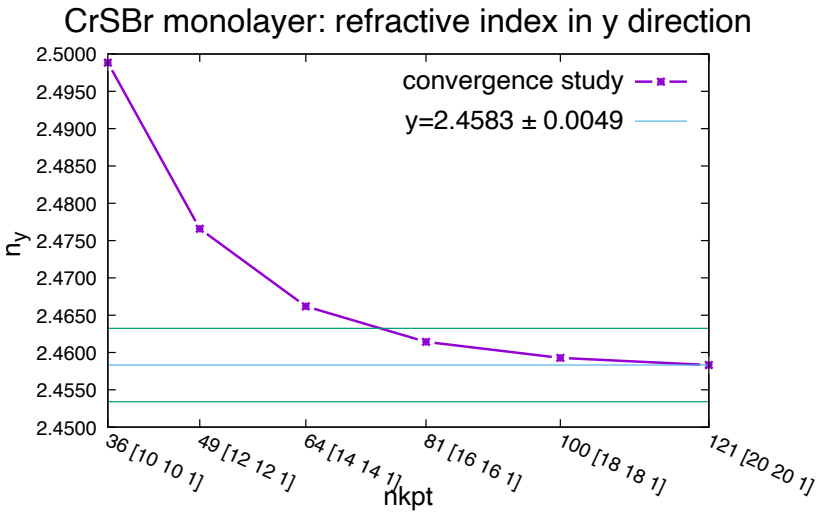

Fig. 2.17.: Convergence study of n_y with respect to kpoints for monolayer CrSBr in DFT+U, $U = 6$ eV and $J = 0.8$ eV. Obtained value kpoints $= [16\ 16\ 1]$.

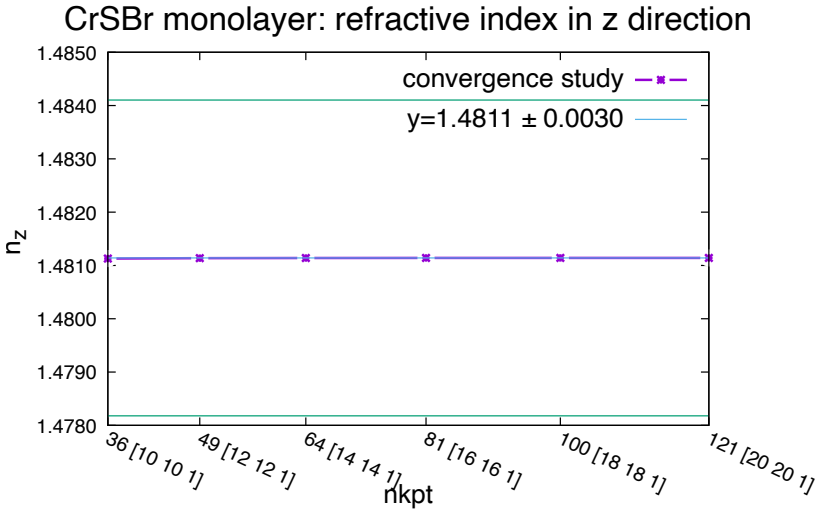

Fig. 2.18.: Convergence study of n_z with respect to kpoints for monolayer CrSBr in DFT+U, $U = 6$ eV and $J = 0.8$ eV. Obtained value kpoints $= [10\ 10\ 1]$.

Vacuum

The convergence studies of n_x, n_y and n_z (kpoints $= [16\ 16\ 1]$ and ecut $= 25$) with respect to c are shown in Figure 2.19, Figure 2.20 and Figure 2.21, respectively. Note $c > 11.96$ Å diverged.

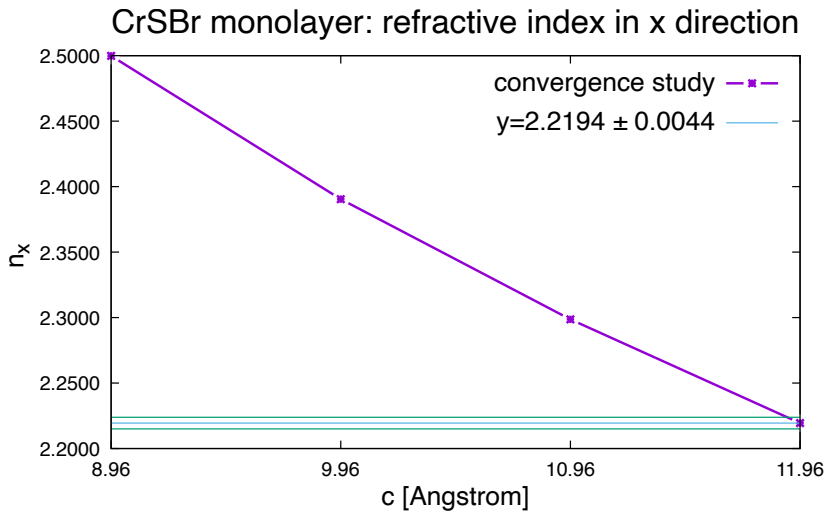

Fig. 2.19.: Convergence study of n_x with respect to c for monolayer CrSBr in DFT+U, $U = 6$ eV and $J = 0.8$ eV. Obtained value $c = 11.96$ Å.

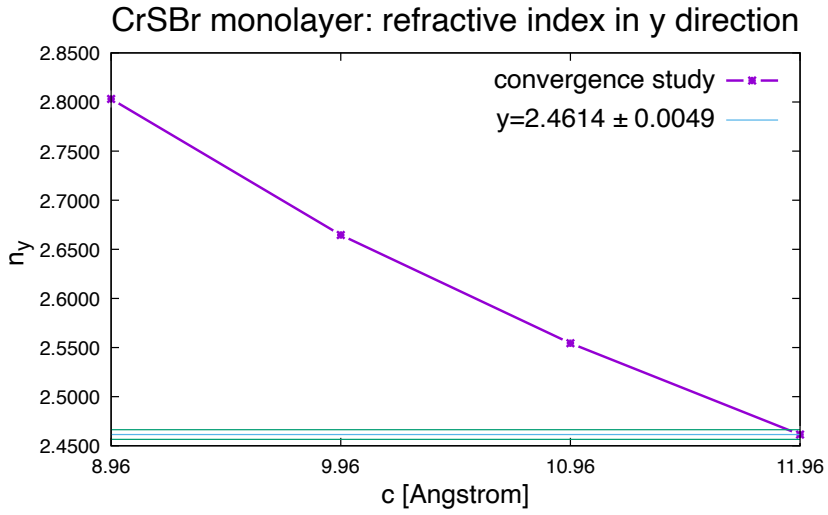

Fig. 2.20.: Convergence study of n_y with respect to c for monolayer CrSBr in DFT+U, $U = 6$ eV and $J = 0.8$ eV. Obtained value $c = 11.96$ Å.

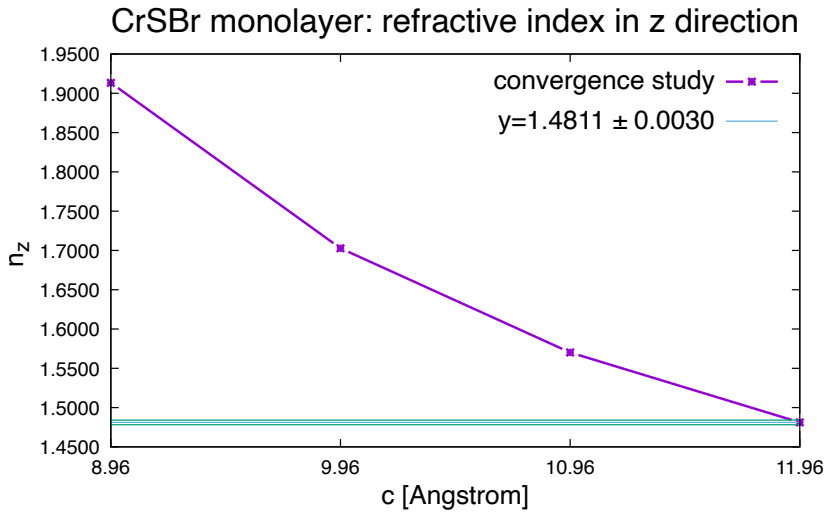

Fig. 2.21.: Convergence study of n_z with respect to c for monolayer CrSBr in DFT+U, $U = 6$ eV and $J = 0.8$ eV. Obtained value $c = 11.96$ Å.

Discussion

The refractive index converged at a value of ecut $= 25$ and kpoints $= [16\ 16\ 1]$. Unfortunately, it was impossible to have the refractive index converge with respect to the size of the vacuum slab to represent a monolayer. When a lattice parameter of $c = 12.96$ Å was considered, the electric field perturbations no longer converged. The found refractive index is, therefore

$$n_x = 2.2194, \quad n_y = 2.4614, \quad n_z = 1.4811 \tag{2.2}$$

2.2.2 DFT with Norm-Conserving (NC) and scissor cut

Since it was not possible to breach beyond $c = 11.96$ Å in the DFT+U scheme, a second attempt was made to overcome this obstacle by performing DFT calculations with norm-conserving LDA potentials [34] with a scissor cut (= band $\text{gap}_{\text{DFT+U}}$ − band $\text{gap}_{\text{NC}} = 1.13$ eV). Since the convergence study for DFT with NC is analogous to the DFT+U case, only the results and important graphs shall be shown here; the rest can be found in the appendix A.2.

After some trial and error, a starting point that converged was ecut $= 40$ and kpoints $= [12\ 12\ 1]$ and $c = 13.96$ Å (since we want to try somewhere above $c = 11.96$ Å). The convergence study for the refractive index converged at ecut $= 55$. The convergence study for the kpoints was terminated at a certain point because the computational cost became too demanding. A least squares fit with three variables was made to all but the last calculated data points and is shown in Figure 2.22.

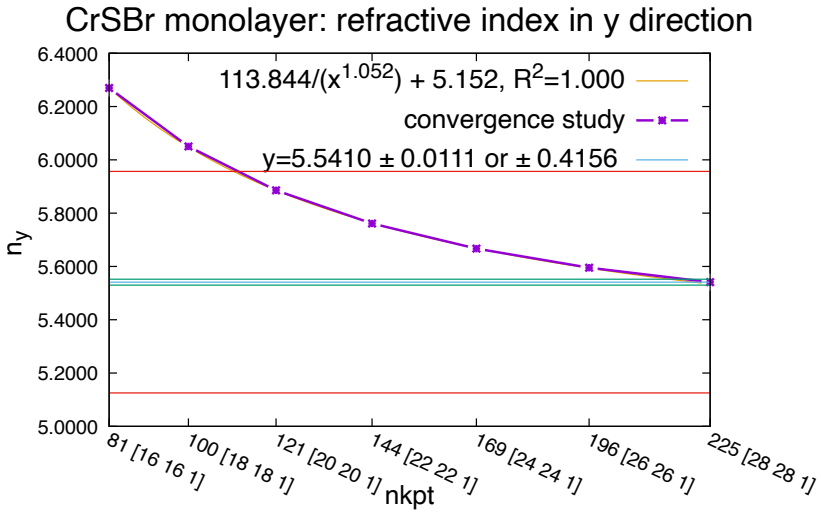

Fig. 2.22.: Convergence study of n_y with respect to kpoints for monolayer CrSBr in DFT + scissor cut. Along with a least square fit to all points except kpoint $= [28\ 28\ 1]$. The parameters of the fit and their errors are $a = 113.844 \pm 12.28$, $b = 5.15237 \pm 0.01946$ and $c = 1.05204 \pm 0.02831$. Obtained value kpoints $= [20\ 20\ 1]$ at an error of 7.5%.

By extrapolating the fit, it is possible to obtain a converged value around the point $[44\ 44\ 1]$. This is way too high to be feasible. By not including the value $[28\ 28\ 1]$ in the fit, a very rudimentary assessment can be made about the fit's predictive power. The value $[28\ 28\ 1]$ lies above the fit. This implies that the fit descends slower than what is actually observed. The converged value might therefore be lower than $[44\ 44\ 1]$, but this is still way too high. It was therefore opted to accept a higher error of 7.5%, and with this, the value $[20\ 20\ 1]$ was chosen to continue. The vacuum did also not converge, and it seems to be far away from converging, no fit was done. The value $c = 18.96$ Å is taken. The found refractive index is, therefore

$$n_x = 2.2215, \quad n_y = 5.0798, \quad n_z = 1.2428 \tag{2.3}$$

2.2.3 Conclusion

In this section, an attempt was made to calculate the refractive index of a monolayer of CrSBr. It was necessary to consider DFT+U calculations with spin polarisation. During the calculations in this scheme, it was not possible to increase the vacuum high enough to have it converge. A different approach of NC potentials with a scissor cut was performed to attempt to overcome these hurdles. While this second approach could theoretically handle these problems, it came at an enormous computational cost. On top of this, as seen from Table 2.1, the values between the two approaches differ a lot. Note that all values are taken at $c = 11.96$ Å, so they are comparable.

	n_x	n_y	n_z
DFT+U	2.2194	2.4614	1.4811
DFT+U$= 0$	2.6903	6.6106	1.5079
NC+sciss	2.6901	6.2954	1.5051

Tab. 2.1.: The refractive index values for CrSBr with $c = 11.96$ Å in three different schemes at their respective converged values.

It seems that U has an enormous impact on the results. As mentioned earlier, one possible reason is that when applying a U, there is only a direct band gap. This claim is based on section 2.1, and the band structure was not recalculated with the newly obtained values. The band structure should be checked, which can be done in future work. The values obtained from the DFT+U case also seem more reasonable than the others; a refractive index of 6.2954 seems rather high. Because of this, a test was performed on ecut $= 55$ and kpoints $= [12\ 12\ 1]$ and $c = 13.96$ Å to assess the impact of the scissor cut (inputs files are in section A.3). The results are

$$\text{no sciss cut:} \quad n_x = 2.5183, \quad n_y = 6.9668, \quad n_z = 1.3887 \tag{2.4}$$

$$\text{with sciss cut:} \quad n_x = 2.5122, \quad n_y = 6.9644, \quad n_z = 1.3853 \tag{2.5}$$

Taking all this into account, the DFT+U values will be considered as correct. Unfortunately, as mentioned in the beginning of this section, it is not possible to compare these values to the literature.

3 Fabrication

> *Don't wish it was easier, wish you were better.*
>
> **— Jim Rohn**
> (American entrepeneur)

The goal of fabricating a twisted CrSBr nanostructure and visualizing its Moiré pattern involves several steps. As discussed in previous section, CrSBr is a vdW material, therefore it is possible to isolate individual few atom-thick layers. Such monolayers can then be stacked on top of each other with a relative angle. As mentioned in Sec. 1.4, this angle might manifest new properties like superconductivity in twisted graphene. The first fabrication step consists of finding an optimized strategy to easily obtain such layers. After this, these layers should be assembled on top of one another. Since obtaining monolayers of CrSBr is already challenging in and of it self, maximizing the monolayer quality is therefore beyond the scope of this thesis. Needless to say, the cleaner, more pristine the monolayer, the better.

3.1 Monolayer fabrication techniques

In the field of 2D materials, there are two main roads to obtain monolayer out of a 2D material, bottom-up approach and top-down approach respectively. The choice of the fabrication method usually relies on the 2D material of interest and the subsequent application.

3.1.1 Bottom-up approach

This process entails attaching smaller molecules, such as hydrocarbons, to a substrate in order to produce graphene or its derivatives. Many of these processes are very interesting for later commercial applications of 2D materials, since these techniques can

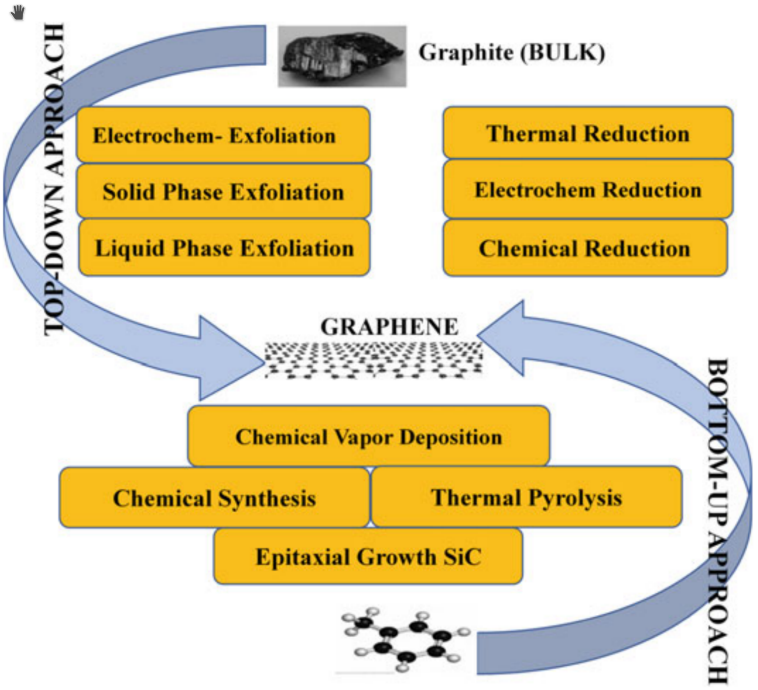

Fig. 3.1.: Different techniques within the bottom-up and top-down approaches for graphene-like 2D materials. Figure taken from [9].

often be scaled and controlled on an industrial scale. On the other hand, despite many improvements over the years, the quality of monolayers obtained by applying this strategy is inferior to most top-down approaches. [9] Chemical Vapor deposition (CVD) is one of the most popular methods in the scientific community for fabrication of single to few layers of nanosheets in either crystalline or amorphous configurations in large sizes. CVD targets molecules from conducting materials with high precision and extremely controlled parameters like temperature, pressure, flow rates, etc. However in some particular cases it turns out that the imperfections of CVD can be repaired afterwards. For instance, when MoS_2 is grown via CVD there will be inevitable Sulfur vacancies. These can be repaired by the introduction of thiol-group-containing molecule (i.e. a sulfur containing group). [11]

3.1.2 Top-down approach

Among the different approaches shown in Figure 3.1, the most commonly used top-down procedure, due to its simplicity and low costs, surely is the mechanical exfoliation - also known as Scotch tape method. This technique, introduced for the first time by Geim and Novoselov in 2004 [27], consists in cleaving away single or multiple 2D material layers from a bulk crystal by employing commercial scotch tape. The cleaved single/multilayer flakes are then transferred on top of a desired substrate, usually Silicon (Si) wafers covered by thermal Silicon Oxide (SiO_2) of ~ 300 nm thickness. The choice of the substrate is motivated by its desirable property of having high contrast in the reflectance between the presence of a flake or not. This aids in the optical inspection of the quality and or thickness of the flake. A second nice property is that this oxide layer makes the surface an insulator. This is useful for device fabrication, such as field-effect-transistors (FET).

The process is shown in Figure 3.2. To improve the yield of this method, the substrate can be pre-treated to make it more adhesive, by performing oxygen plasma cleaning. In the case of SiO_2 substrates, this removes natural contamination passivisation layers that terminate the surface and makes the substrate change from hydrophobic to hydrophilic. [16]

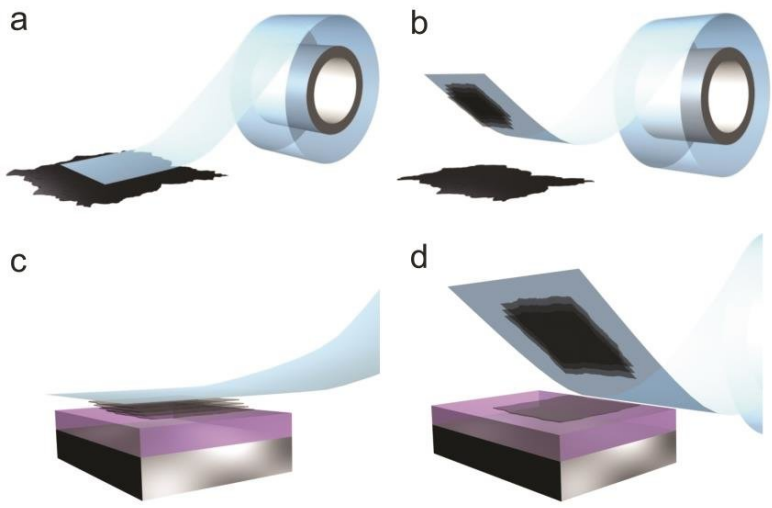

Fig. 3.2.: Schematic of the simple mechanical exfoliation process. Figure taken from [11].

Since the material comes from bulk crystals, which are relatively easy to grow without defects, the resulting multilayer flakes are of pristine quality. This is due to the fact that

the few layers have not been in contact with the scotch tape glue directly, but indirectly via the other layers of the material. The main benefits of this technique is thus the resulting quality of the flakes and the ease and cost of fabrication. All these factors make it hence ideal for research purposes. The main drawbacks are the possible size of the resulting flakes, these tend to be not as large (few micrometers maximum), and the reproducibility is low for the technique. Hence why this technique is not suitable for commercial purposes.

3.2 Au-assisted exfoliation

The main novelty from recent years is using gold to perform exfoliation of 2D materials. The first group to investigate these unique properties of gold was Velickyét al. in 2018 [42], who successfully and reliably exfoliated large-areas of the TMDC (Transition-Metal-Dichalcogenide) MoS_2 on fresh gold. [42]

The main advantages of using gold (Au) substrates for exfoliating 2D materials are reported in Figure 3.3. Indeed, it is shown that exfoliating on a Au evaporated substrate gives on average much larger monolayer flakes with respect to other substrates and metal evaporated substrates (see Figure 3.3, **e**). This is due to the attraction strength of the Au-TMDC interface being strong enough to peel of van der Waals attached layers. However the force is still weak enough to not form covalent bounds with the monolayer so as not to alter the TMDC monolayer structure. This unique property of Au is attributed to its large electronegativity (large binding energies) and its strain inducing capabilities in TMDCs (Figure 3.3, **f**). Both are necessary, since platinum (Pt) and palladium (Pd) have larger electronegativity than both Au and silver (Ag) but seem to attract less monolayers (Figure 3.3, **e**). On top of this, because even the slightest imperfection is important on the atomic scale, Au's relative inertness is also very appealing. Nevertheless, to make full use of Au's capabilities, using fresh Au is detrimental as can be seen from Figure 3.3, **d**.

3.3 Quality of the flakes

Most advanced monolayer fabrication techniques use additional substances to increase properties of the techniques like reproducibility, achievable fabrication size, monolayer shape versatility, transferability etc. However, these improvements often come at a price

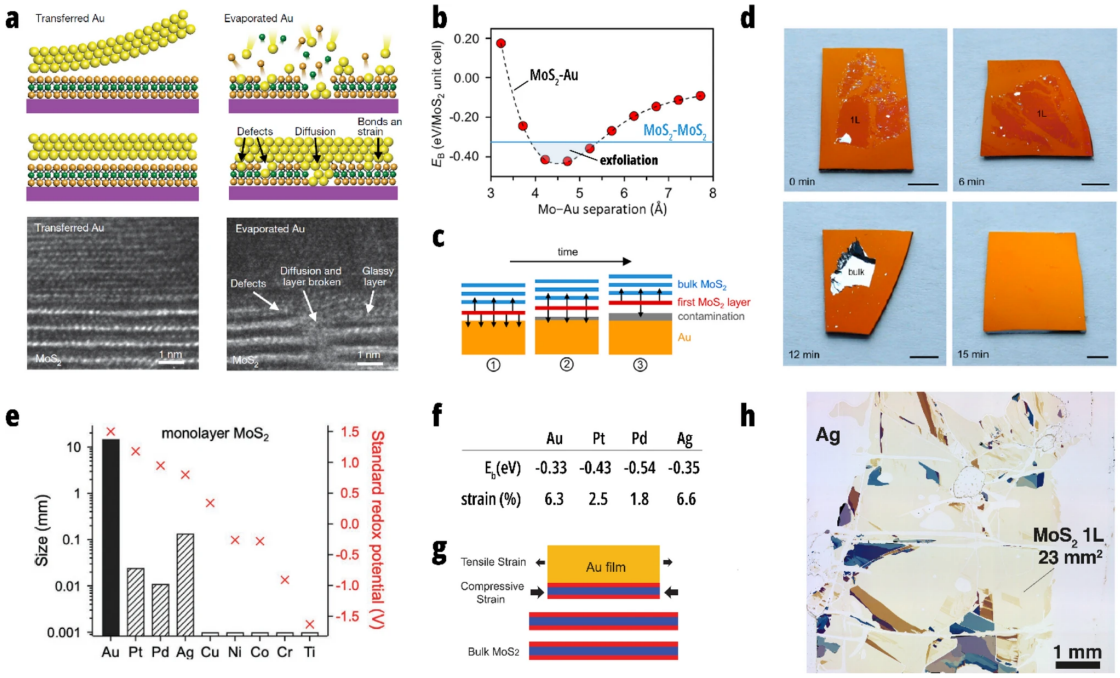

Fig. 3.3.: Insights into the mechanism of metal-mediated exfoliations. **a** Two different principles of forming the Au-MoS_2 interface are detailed. Transferred Au (left), a smooth and clean Au surface is brought into conformal contact with MoS_2. Evaporated Au (right) relies on direct deposition of (high-energy) Au on MoS_2, leading to different interaction pathways, also evident in the defects and damages in the TEM cross-section image below. **b** The vdW interaction mediated exfoliation via overcoming the (blue) interlayer MoS_2 binding energy is depicted (curve from vdW DFT calculations). The strict dependence on the MoS_2-Au separations suggests a smooth and clean gold surface is key to unlock this exfoliating vdW interaction regime, as depicted in (**c**). Here, even the build-up of a molecular contamination layer over time (e.g., air-borne carbohydrates from oil pumps running in the lab) can hinder the exfoliation, which degraded the exfoliation performance within minutes (**d**). Scale bars in d correspond to 5 mm. **e** The exfoliated single layer size for other metals than Au is shown. A decrease in nobility (indicated via standard redox potential) is apparent. **f** Computed Metal-MoS_2 binding energies (optb88b-vdW-DF) and compressive strain values applied to the metals to match the lattice constant of MoS_2. Mechanism of strain-mediated exfoliation via disruption of the layer stacking registry at the metal-TMDC interface. **h** Optical micrograph showing silver-mediated MoS_2 exfoliation performing on par with gold via a low-temperature (150 °C) annealing. Figure taken from [14].

of increased contamination. For instance in most Au-assisted fabrication techniques, once a monolayer is successfully exfoliated, the Au needs to be removed later on via etchants which can induce contamination or defetcs. A list of common contaminations or defects as a result of transfer or fabrication methods can be found in Table 3.1.

Drawbacks	Possible causes	Effects	Characterization	Possible solutions
Wrinkles and cracks	Thermal fluctuations.	Wrinkles can greatly enhance PL signal.	Optical microscopy, PL, SHG, AFM, STM and SEM.	Use more robust support layer.
	Difference in surface energy between support and 2DLM.	Lower electronic mobility.		Match thermal properties (i.e. TEC) of substrate and 2DLM.
	Bubbling in a solution or from capillary forces (additional mechanical stress).	Cracks can cause open circuits.		Avoid mechanical peeling.
	Evaporation of solvents used to remove the support.			
	Use of support with low viscoelastic properties.			
Trapped bubbles	Trapped water or residue from chemical etchants.Trapped air pockets from dry transfer.	Weaker proximity effects and interlayer excitons.Enhanced strain.	STM, SEM and AFM. PL for heterostructures.	Control contact angle and merging time.Mild annealing during and after transfer.
Polymer residues	Residue remains after removal of support.	Change in doping. Decrease of electronic mobility.	Optical microscopy, STEM and AFM.	Annealing. Dissolve in organic solvents. Contact-mode AFM can 'sweep' scan area free of residues. Pre-cleaning PDMS by UV/ozone.

Tab. 3.1.: An overview of the various drawbacks associated with different transfer techniques, together with the effects on material properties, and methods to characterize and solve these drawbacks. Table taken from [44].

It goes without saying that preventing contamination is always preferred over cleaning or repairing defects of the monolayer afterwards. For this reason, it is preferable to perform the fabrication in a clean room environment. In some circumstances, it might even be required to execute these techniques under an inert ambient environment like nitrogen gas atmosphere in a glovebox or even in vacuum. When fabricating monolayers for heterostructures, those monolayer often need to be transferred. Depending on what contaminations are tolerable, different transfer techniques can be used.

3.4 Transfer Methods

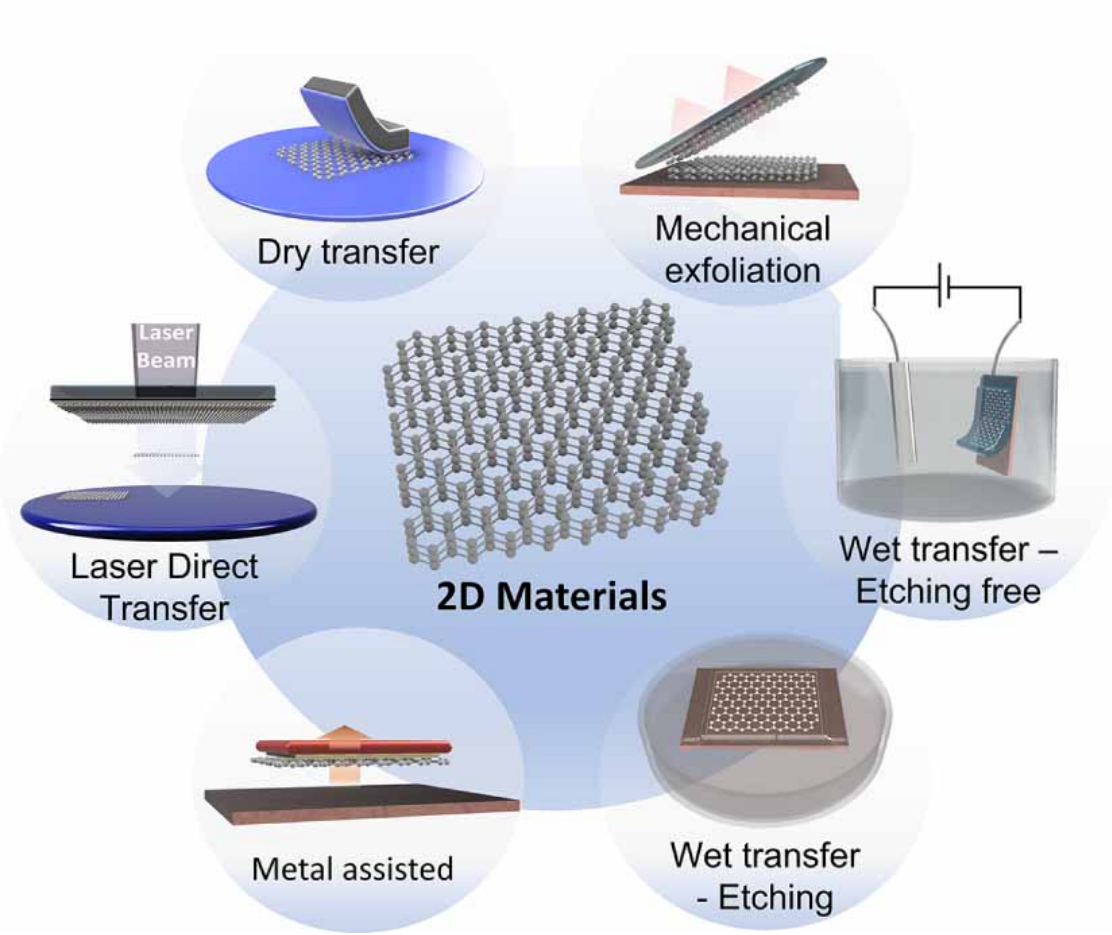

Fig. 3.4.: Visualisation of some of the main transfer methods for two-dimensional materials. Figure taken from [8].

Depicted in Figure 3.4 and reported in Table 3.2 are several transfer methods with their targeted 2D-material, suitable substrates, carrier substrates and pros and cons. This list does not contain all possible transfer methods, as many variations have spawned over time. Many transfer techniques are tailored towards a specific quality or property. For instance, material carrier mobility, reproducibility, cleanliness, easy-of-use, final substrate topography etc.

Transfer Technique	2D materials	Suitable substrates	Carrier substrate	Advantages and limitations
Chemical etchant assisted wet transfer (Wet)	i. Graphene ii. MoS_2 iii. hBN	i. CVD on metal ii. CVD on SiO_2	i. PMMA ii. Paraffin	+ Less mechanical damages + Reduced strain effect on the flakes + >8-inch graphene transfer + Compatible with the roll-to-roll process + High mobility for graphene using Paraffine as polymeric supporting layer - Polymer residue - Difficult to scale up
Etchant free (Electrochemical bubbling transfer, Wet)	i. Graphene ii. MoS_2 iii. hBN iv. WS_2 v. MoS_2	Metal growth substrates	i. PMMA ii. PVA iii. EVA	+ Cost-efficient because of metal recycle + Faster process than chemical etchant assisted wet transfer + Compatible with the roll-to-roll process for graphene and WS_2 - Bubbles may crack the samples
Capillary force (Wet)	i. MoS_2 ii. WS_2 iii. WSe_2	i. Hydrophilic substrates like SiO_2 growth substrates ii. Hydrophilic substrates like sapphire growth substrates	i. PDMS ii. PS iii. PMMA	+ Easy identification of monolayer + High mobility - Surface tension induced by the capillary force

Mechanical Exfoliation (Dry)	i. Graphene ii. MoS_2 iii. WS_2	i. Metal growth substrate ii. SiO_2 growth substrates	i. MoO_3 ii. EVA iii. PDMS iv. PMMA v. hBN vi. PVA	+ Roll-to-roll compatible transfer + High mobility + Less polymer residue using the MoO_3 and EVA adhesion layers + Recycle of the growth substrates + For the vdW peak up method using hBN as adhesion layer there is the cleaner interface + Fabrication of 2D heterostructures using optical microscope system + 2D material transfer to a substrate with pre-fabricated electrode structures such as Source and Drain - Mechanical damages - It is difficult to completely remove adhesive layers
Chemical etchant assisted dry transfer (Dry)	i. Graphene ii. hBN	Metal growth substrate	i. PDMS ii. PVA iii. PSAF	+ Compatible with the stamping technique + No Polymer residues - Use of specific chemicals for etching the growth substrate
Laser-induced forward transfer	i. Graphene ii. MoS_2	Pre-transferred substrates	i. Ni ii. Cu iii. PMMA	+ Easy patterning + Less polymer residue + Controlling the size of the transferred material surface by adjusting the laser beam's size + It is possible to manufacture larger surfaces by transferring small pixels of 2D materials through digital printing + Transfer to the target wafer without any adhesion or supporting layer - Need for a pre-transfer method before laser transfer
Metal Assisted Transfer	i. MoX_2 ii. Graphene iii. hBN iv. WSe_2 v. $MoSe_2$	i. SiO_2 growth substrate ii. CVD metal growth substrate	i. Cu ii. Au iii. Ni	+ Transfer without leaving polymer residues + No wrinkling or surface imperfections - Use of chemicals for etching the metallic carrier adhesive layer

Tab. 3.2.: A comparative analysis of various transfer methods for 2D materials. Table taken from [8]

3.4.1 Semi-wet transfer

This transfer technique uses water soluble polymer (ex. Polyvinyl Alcohol, PVA) in combination with a non-water-soluble polymer (ex. Polymethylmethacrylaat, PMMA) to detach a flake from a desire substrate. Substrates like SiO_2 are normally preferred because they make it easy to optically identify interesting flakes, as mentioned earlier and will be shown further on. Mechanically exfoliation on translucent polymers alone does not have this benefit. Once optically identified, flake can be transferred to a different flake or substrate by dissolving the water soluble polymer. The process is shown in Figure 3.5.

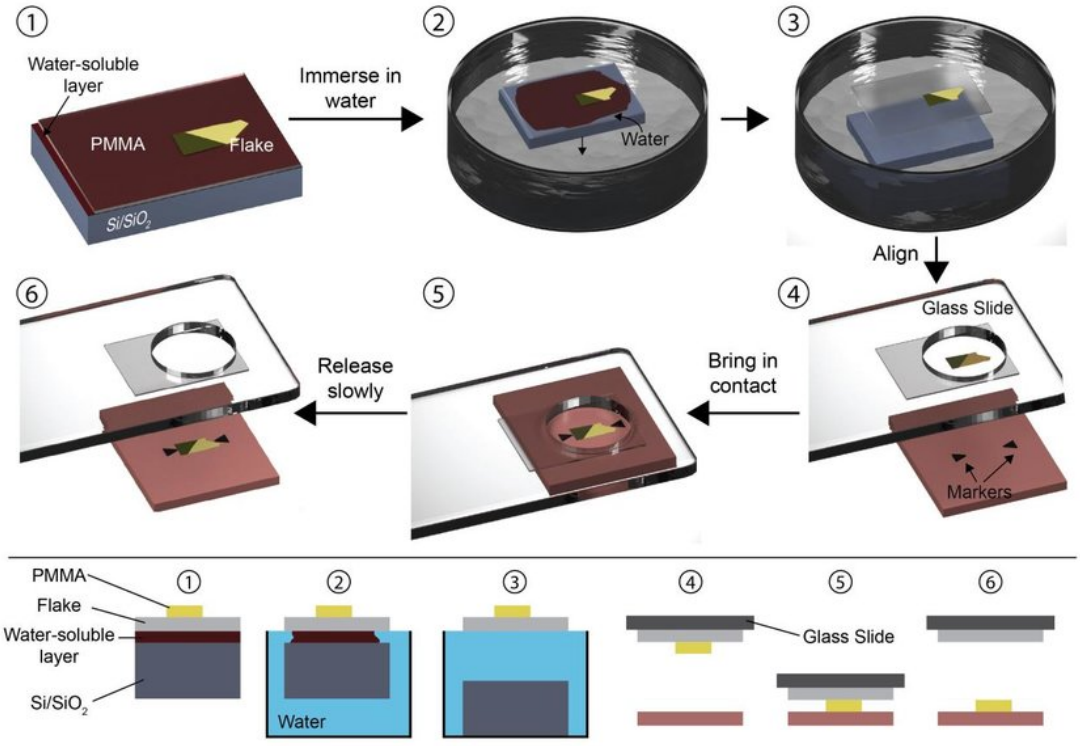

Fig. 3.5.: The PMMA carrying layer transfer method. The designated flake to be transferred is exfoliated onto a Si/SiO_2 substrate which has been coated with a water-soluble polymer layer and PMMA (1). The stack is then immersed in water (2) where the water-soluble layer can dissolve leaving the PMMA layer carrying the flake floating on the water surface (3). The PMMA is then attached to a glass slide connected to a micromanipulator with the flake facing down (4). With the help of a microscope the flake is aligned with the target substrate and is then brought in contact (5). By gently separating the PMMA from the final substrate the flake get transferred. Figure taken from [12].

The thicknesses of the two different polymers should be chosen to optimise optical contrast to maximise the visibility of flakes. [2, 3] The contrast C is defined as the relative intensity of reflected light in the presence ($n_1 \neq 1$) and absence ($n_1 \neq n_0 = 1$) of graphene

$$C = \frac{I(n_1 = 1) - I(n_1)}{I(n_1 = 1)} \tag{3.1}$$

where the intensity (I) is the reflected intensity from a configuration of the different thin film layers. This can be calculated using transfer matrix method, which is a generalised version of the Fresnel equations [6]:

$$r_s = \frac{n_1 \cos\theta_1 - n_2 \cos\theta_2}{n_1 \cos\theta_1 + n_2 \cos\theta_2} \quad , \quad r_p = \frac{n_2 \cos\theta_1 - n_1 \cos\theta_2}{n_2 \cos\theta_1 + n_1 \cos\theta_2} \tag{3.2}$$

$$t_s = \frac{2n_1 \cos\theta_1}{n_1 \cos\theta_1 + n_2 \cos\theta_2} \quad , \quad t_p = \frac{2n_1 \cos\theta_1}{n_2 \cos\theta_1 + n_1 \cos\theta_2} \tag{3.3}$$

The transfer matrix describes the behaviour of light within an individual layer and is then:

$$M_n \equiv \begin{pmatrix} e^{-i\delta_n} & 0 \\ 0 & e^{i\delta_n} \end{pmatrix} \begin{pmatrix} 1 & r_{n,n+1} \\ r_{n,n+1} & 1 \end{pmatrix} \frac{1}{t_{n,n+1}} \tag{3.4}$$

The behaviour for the entire system can then be described by:

$$\begin{pmatrix} 1 \\ r \end{pmatrix} = \tilde{M} \begin{pmatrix} t \\ 0 \end{pmatrix} \tag{3.5}$$

with

$$\tilde{M} = \frac{1}{t_{0,1}} \begin{pmatrix} 1 & r_{0,1} \\ r_{0,1} & 1 \end{pmatrix} M_1 M_2 \cdots M_{N-2} \tag{3.6}$$

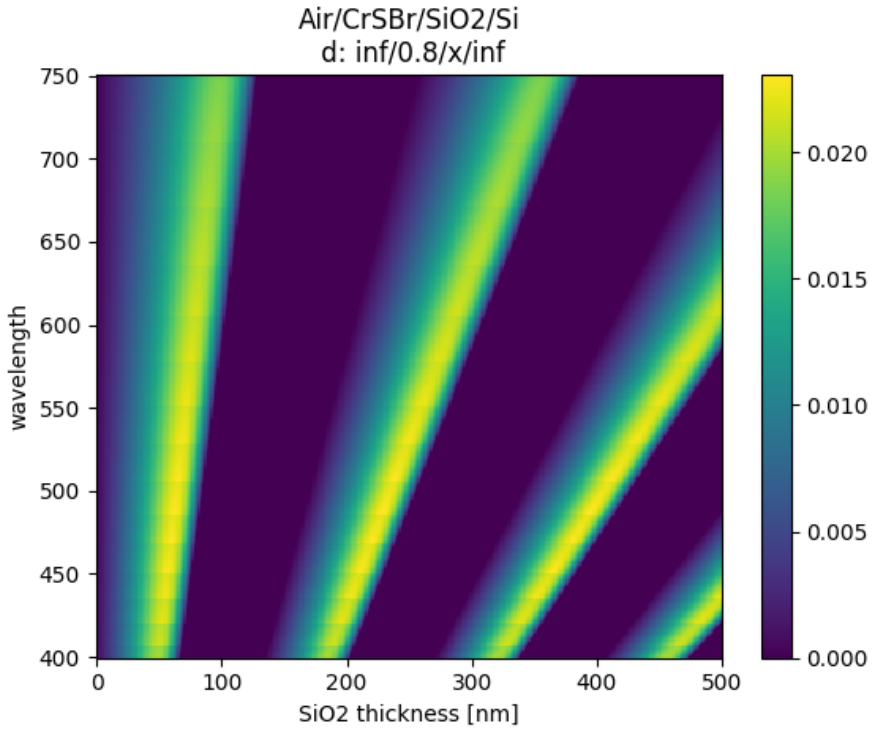

Fig. 3.6.: Optical contrast for CrSBr when sweeping over wavelength and SiO_2 thickness.

3.5 Fabrication of twisted CrSBr

Twisted CrSBr consists in a stack of two CrSBr flakes overlapped with a relative misalignment. In order to fabricate this structure, it is necessary to exfoliate thin flakes of CrSBr and subsequently transfer one on top of the other rotated by a certain angle. For simplicity and quality reasons, mechanically exfoliation shall be performed. Transfer of the obtained flakes shall be done using PPC (Polypropylene carbonate).

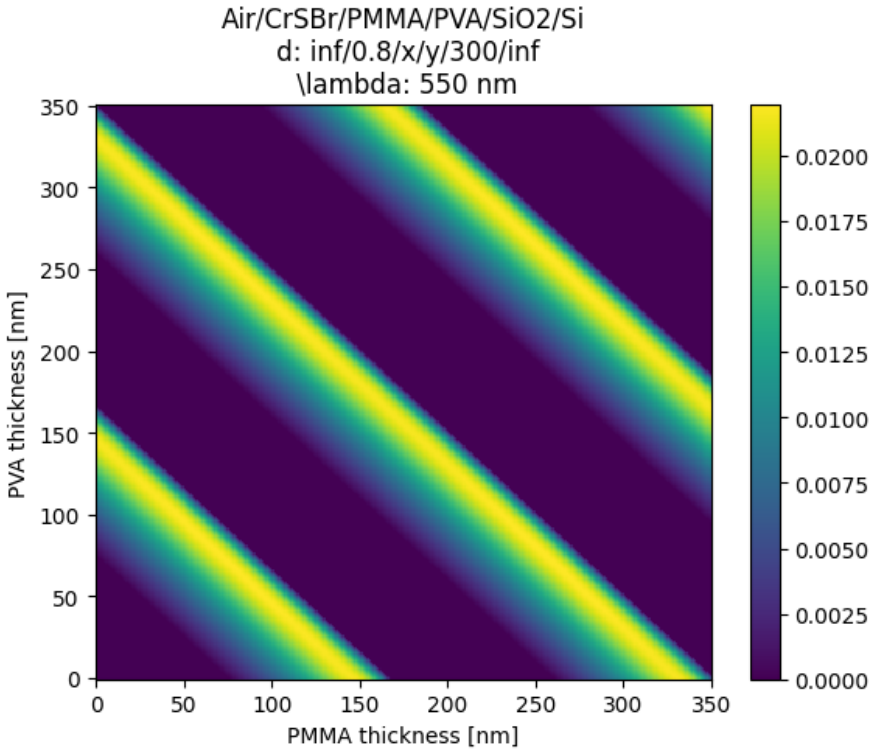

Fig. 3.7.: Optical contrast for CrSBr when sweeping over PMMA and PVA thickness at a wavelength of 550 nm. This gives the ideal optical identification conditions for the technique described in Figure 3.5.

3.5.1 Substrate preparation

Before performing the mechanical exfoliation, a Si substrate with a 285 nm SiO_2 layer will be cleaned thoroughly. This is standard practise in the field and is done by first blowing drying it with a nitrogen gun. Next, the substrate is sonicated for 10 minutes in an acetone bath. This is followed by a 10-minute sonication in a isopropanol bath, and a 5-minute sonication in a deionised water bath. The substrate is then removed from the water and blow dried with a nitrogen gun. To remove excess water it is annealed for 2 minutes at 150°C on a hotplate. Optionally this is followed by a 2-minute O2-plasma cleaning. This last step uses highly reactive oxygen radicals created under UV-rays to remove organic compounds in a dry fashion. On top of this, it activates the SiO_2 terminations of the surface. [16]

For future steps in the fabrication process the substrate will be treated with dodecanol. Submerging of the substrate in dodecanol or drop casting dodecanol on top of the substrate for 2 minutes at $180°$C on a hotplate, leads to the formation of a dodecanol self-assembled monolayer (SAM) on top of the substrate. [19] The thickness of the SAM is less than 1 nm; being therefore so thin, this added layer doesn't change the overall refractive properties. Which is desirable since the 285 nm SiO_2 layer is chosen (among other reasons) because of ideal optical identification properties as mentioned before. It is possible to identify the success of the treatment by checking the hydrophobicity of the surface, since dodecanol makes it extremely hydrophobic.

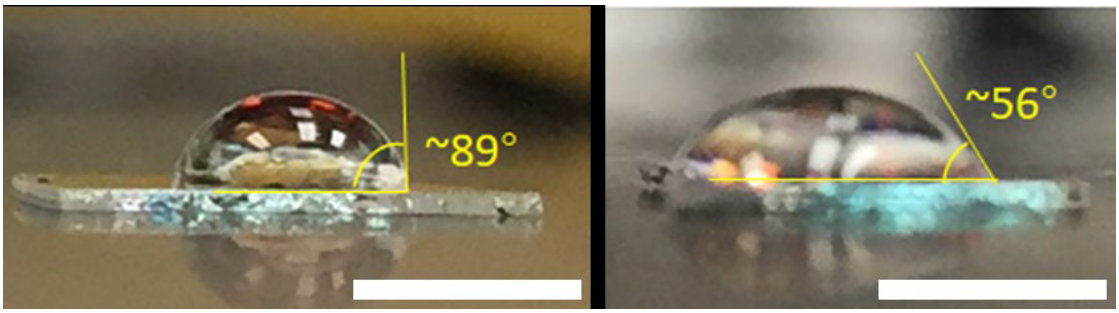

Fig. 3.8.: Water contact angle on SiO_2 surface with (left) and without (right) dodecanol self-assembled monolayer (SAM). The scale-bar is 5mm. Figure taken from [19].

3.5.2 CrSBr flakes exfoliation

Flakes of CrSBr are mechanically exfoliated (see Section 3.1.2) on the prepared substrate. The entire transfer procedure is performed in a glovebox to prevent oxidation of the CrSBr flakes. Since it was impossible to have large enough monolayers, large and relatively thin flakes are used to fabricate a twisted CrSBr device instead. These can be optically identified on 285 nm SiO_2 as the most purple and translucent flakes. An example and chosen flake is shown in Figure 3.9.

To facilitate the assembling of the vdW heterostructure, the thin flake is transferred to a more isolated area. Additionally this can also make it break loose from the thicker areas to which it borders. Transfer after mechanical exfoliation is usually performed using polymers, advantages and disadvantages are listed in Table 3.4. The transfer will be performed by assembling a PPC stamp.

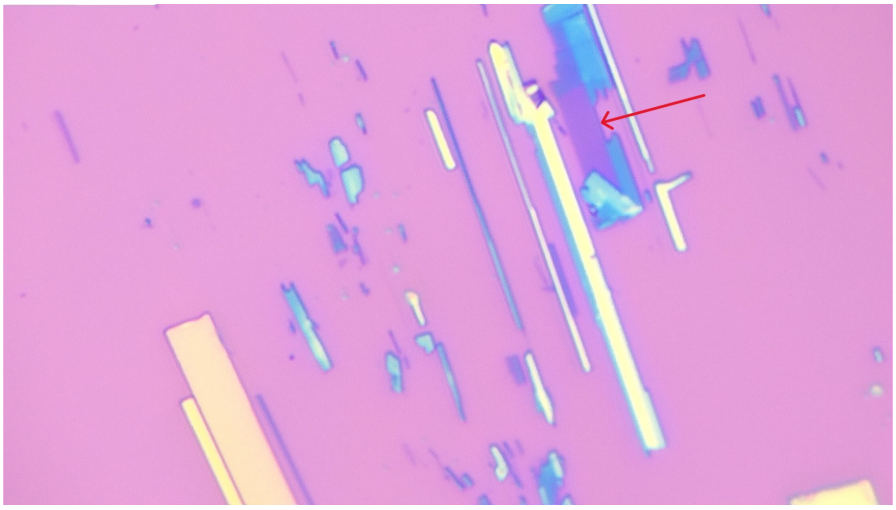

Fig. 3.9.: Optical image of mechanically exfoliated CrSBr on dodecanol treated 285 nm SiO_2 substrate.

3.5.3 Transfer process

PPC is spin coated on a sacrificial Si/SiO_2 substrate to create a thin film of PPC of which the thickness can be controlled by adjusting the rotational speed. This thin film can be lifted of the sacrificial substrate by cutting a hole out of plane scotch tape and placing it on top of the thin film. The hole needs to be small enough in order to support the thin film properly. The thin film will be held up by the tape on the edges and, once the whole structure is lifted off, it will be free standing in the area corresponding to the hole. This free standing PPC thin film is then placed over a small PDMS dome that is attached to a glass slide. The PDMS dome serves multiple purposes. It enables the thin film to bulge out, ensuring that it will come into contact with the flake first. Additionally, it reduces the contact area between the thin film and the substrate, making the transfer more controlled. Lastly, the PDMS will thermally expand when heated, facilitating the contact with the sample.

During the transfer process with polymers, the three most important factors for a successful transfer are temperature, speed and thin film thickness. Onodera et al. investigated this for PVC (i.e. polyvinyl chloride, or plain kitchen clingfilm) [28, 43], but their findings are very general and specific temperature ranges can be adapted based on the glass transition temperature of the polymer used. [24] Their results are shown in Figure 3.10.

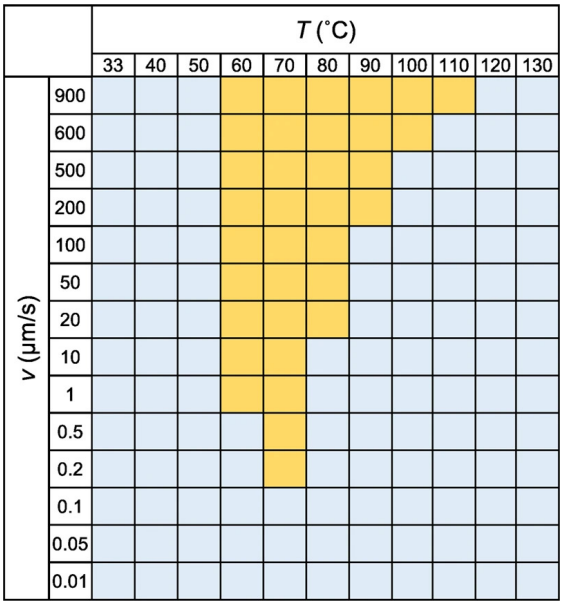

Fig. 3.10.: Results of pickup tests conducted using various values of v and T. Yellow cells indicate successful pickups and light blue cells indicate unsuccessful pickups. Figure taken from [43].

Since the glass transistion temperature of PPC is lower at around $40°$C compared to $70°$C for PVC, the corresponding pickup and release temperatures should change accordingly. The ideal pickup condition is to pickup fast and at $30°$C. The ideal release condition is at around $70°$C and performed slowly. This is in line with the findings from other works. [17, 24]

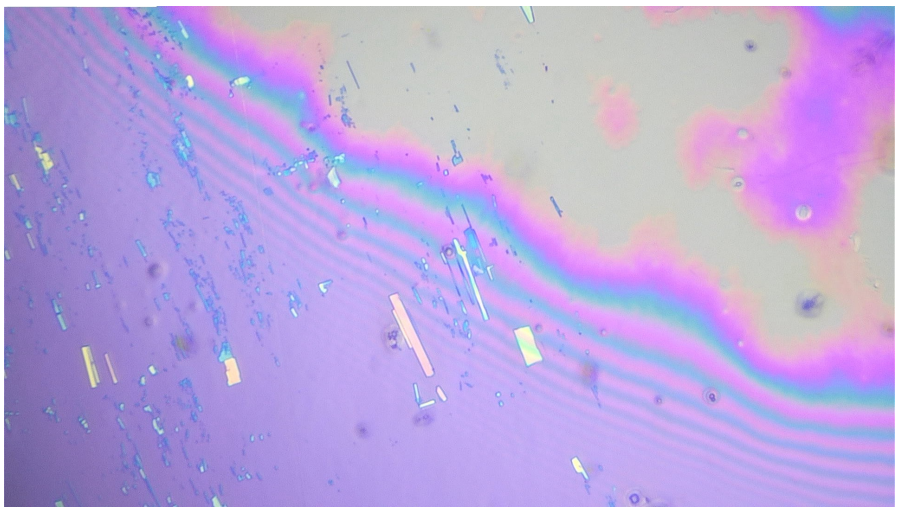

Fig. 3.11.: Zoomed out optical image of just before pickup of the flake shown in Figure 3.9.

In Figure 3.11 an optical image of the pickup process is displayed. The colorful fringes with interference patterns indicate where the PPC border is. Heating to 30°C is performed after contact so that the PPC can extend thermally over the flake for better contact. After contact for a long enough period the stamp is detached from the substrate as fast as possible for best pickup chances. Successful pickup can be checked optically by identifying if the flake remains on either the substrate or the stamp. Once picked up the stamp can be moved to a different area to release the flake. Releasing is done at 70°C and very slowly. The resulting flake is shown in Figure 3.12.

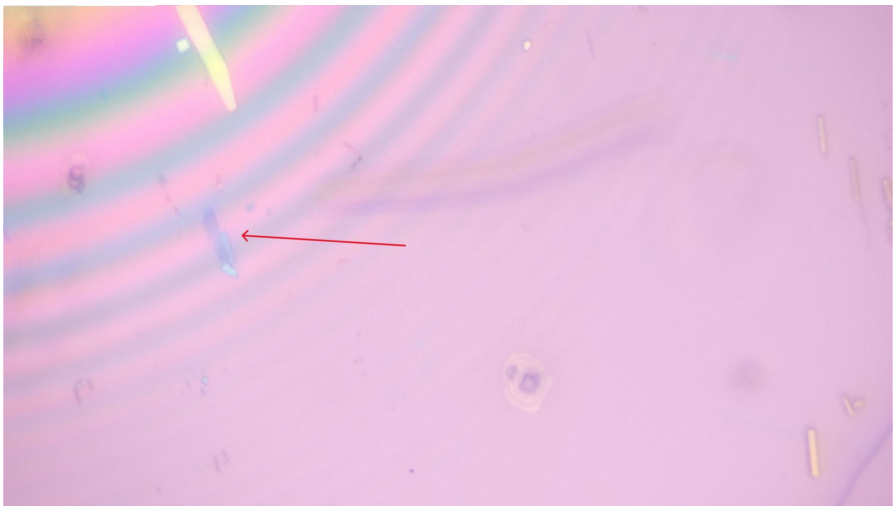

Fig. 3.12.: Optical image just after releasing of the flake at a different location.

Now another flake is put on this isolated flake. A flake that was still left on the stamp was chosen to be released on top of this one. This is shown in Figure 3.13.

After doing so, a piece of the original flake came loose and was picked up unintentionally by the stamp. Nevertheless, the second flake was still released on the original flake and a twisted CrSBr nanostructure was fabricated. When aligning the flakes, a very small angle is desirable since this leads to a very large Moiré wavelength and would therefore be more easily observable. To achieve this, one aims to align them perfectly. However, such atomic precision is not achievable with a human eye it will slightly misalign, leading to the desired outcome. The final structure is shown in Figure 3.14.

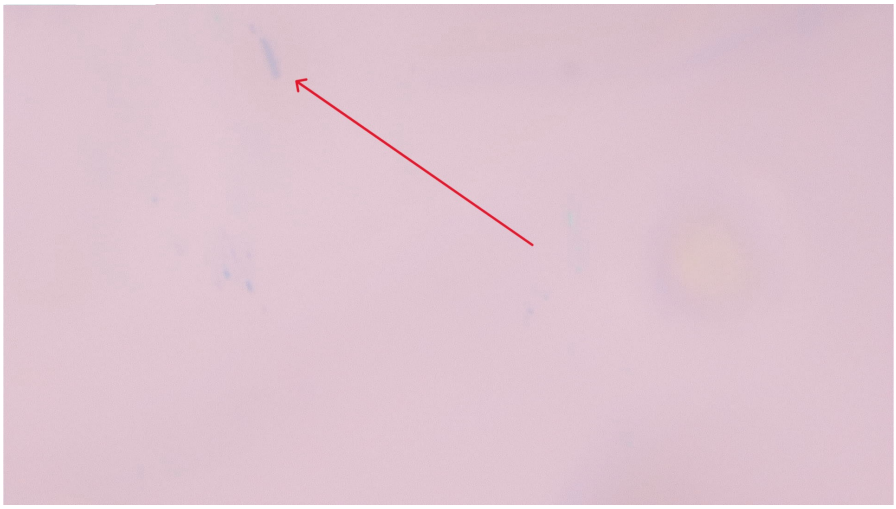

Fig. 3.13.: Optical image of leftover piece of CrSBr that remained on the stamp after first transfer.

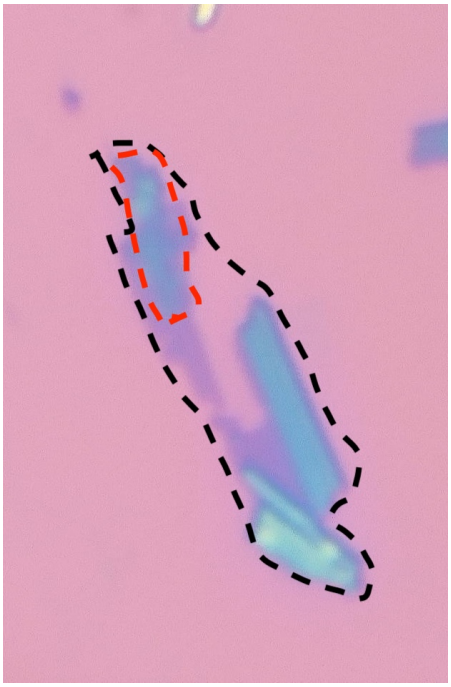

Fig. 3.14.: Optical image of final CrSBr nanostructure.

Characterisation

4

> *Everybody always says:"I would die for you."*
> *Nobody every says: "I would live for you."*
>
> — **Nika Teran**
> (Fellow NTT intern)

4.1 Description of the PFM method

Piezoresponse force microscopy (PFM) is an Atomic Force Microscopy (AFM) mode that allows the mapping of the domain structure in piezoelectric materials (Figure 4.1, left) as well as the measurement of the piezoelectric coefficient. It is thus sensitive to the presence of polarisation domains. By coming close with a tip and applying an electrical field, it is possible to interact with these domain walls. The applied electric field induces a local strain of the piezoelectric material below the tip. If the domain polarisation is out-of-plane, the material will dilate or shrink in the z-direction (Figure 4.1, right), inducing a time-dependent vertical deflection of the cantilever at the excitation frequency that is detected with a lock-in amplifier. This can also be done to check in-plane effects.

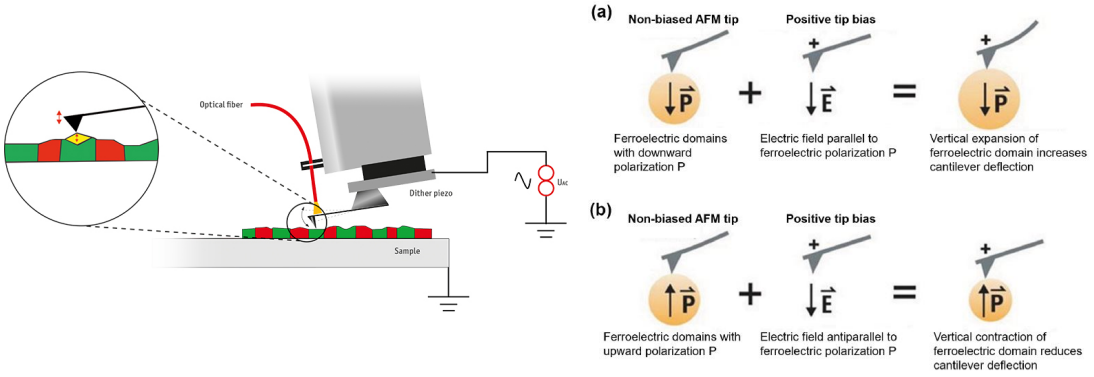

Fig. 4.1.: **Left:** Schematic of the practical workings of a PFM setup. Figure taken from [30]. **Right:** Schematic of the theory behind a PFM signal. Figure taken from [31].

The applied electric field can be described by the following equation:

$$V_{bias} = V_{dc} + V_{ac} \sin(\omega t) \tag{4.1}$$

which can be translated to a deflection of the cantilever:

$$d = d_{33} V_{dc} + d_{33} V_{ac} \cos(\omega t + \phi) \tag{4.2}$$

Thus, measuring this deflection using the classical AFM setup gives us insight into the piezoresponse.

In order to obtain a clear signal by means of this technique, it is thus necessary to use a piezoelectric material Specifically, a twisted bilayer graphene device and twisted CrSBr device are investigated. Although graphene nor monolayer CrSBr or their multilayered variants are piezoelectric, it has been shown that polarisation domains can be formed in the twisted case. [23] One of their results is shown in Figure 4.2. Such phenomenon occurs because flat graphene sheets have planar σ bonds and symmetric π bonds out of the plane. However, when a curvature is present, the bonds bend away from purely planar in character to possess a component of sp3 bonding as opposed to the purely sp2 case of flat graphene. This causes an asymmetric distribution of the electron orbitals and hence gives rise to polarisation.

4.2 Twisted bilayer graphene

The measurements discussed here were performed by the author at the Boltzmann building of UCLouvain with a Bruker Icon Dimension setup.

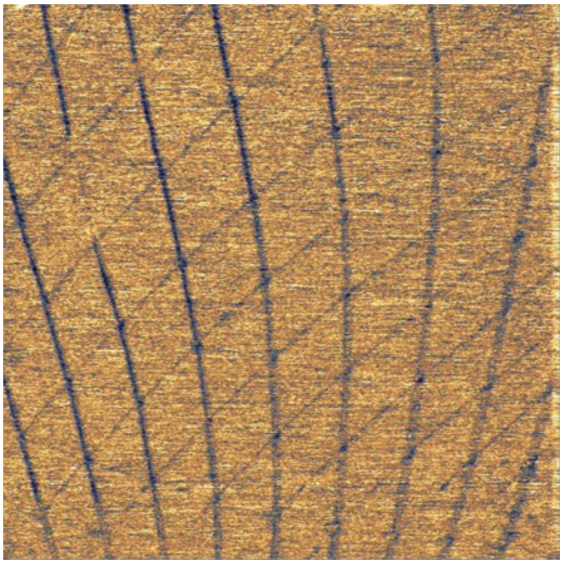

Fig. 4.2.: Qualative image of a PFM measurement of a twisted bilayer device. Figure taken from [23].

Fig. 4.3.: Image of a Bruker setup used to perform AFM measurements. Figure taken from [5].

4.2.1 Setup

Probe

A new PPP-CONTPt (i.e. PointProbe Plus Contact Mode - PtIr5 Coating) was used. This is a rather versatile probe with a nominal resonance frequency of 13 kHz and range [6 - 21] khz. It has a nominal force constant of $0.2\ \frac{\mathrm{N}}{\mathrm{m}}$ and range $[0.02 - 0.77]\ \frac{\mathrm{N}}{\mathrm{m}}$. [33] Note that, as the name implies, it has a PtIr5 coating which is needed for the metallic-like

conductivity of the tip and which is, in turn, crucial to perform PFM measurements. This choice of coating specifically allows for better electrical contact, but it is more prone to wear and tear due to the friction force present in contact mode imaging.

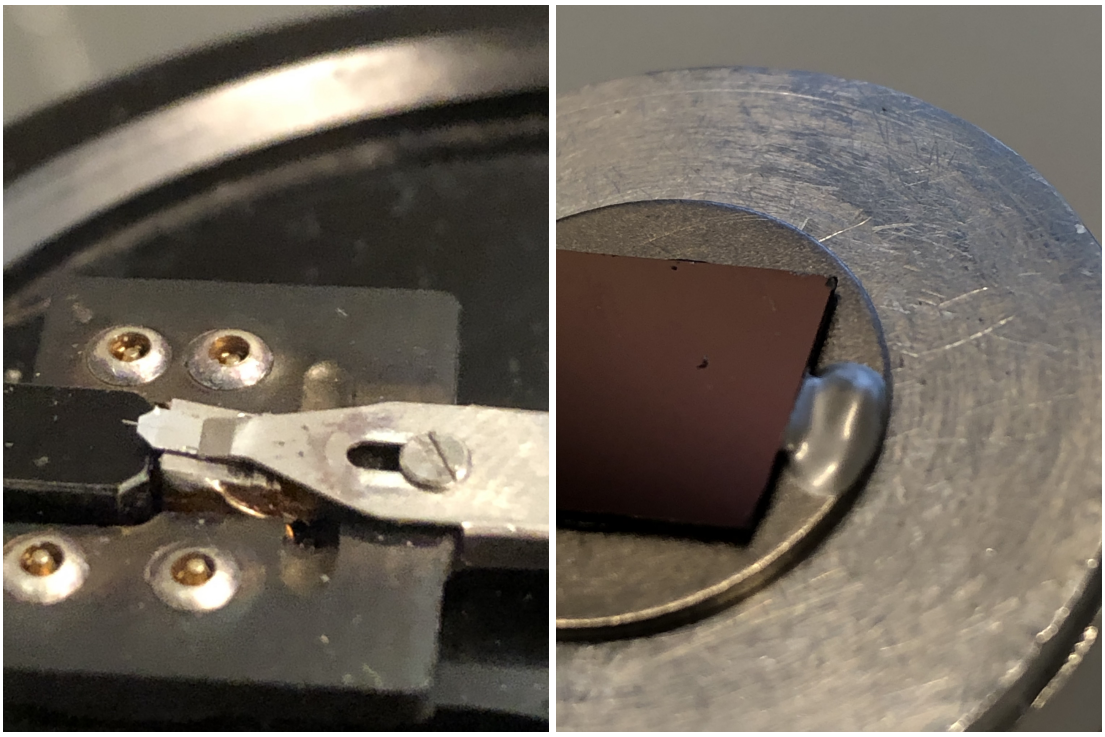

Fig. 4.4.: **Left:** Image of the probe securely placed in the probe holder. **Right:** Image of the sample securely placed on the sample holder.

The probe is carefully placed in the probe holder (as shown in Figure 4.4, right) and then transferred to the Bruker setup. Once installed in the Bruker setup, the laser, cantilever and detector should be positioned accordingly to achieve an optimal signal.

Sample

The sample on which PFM will be performed consists in a twisted bilayer graphene structure located on top of a Si/SiO_2. The sample is secured on the holder with some double-sided sticky conductive carbon tape. However, due to the importance of the substrate being grounded, relatively deep scratches were made on the side of the sample with a diamond cutter. These freshly exposed (non-oxidised) scratches were then covered

with silver paste, which is an excellent conductor. The resulting configuration is shown in Figure 4.4, right.

PFM parameters

Now the three key variables have to be determined that govern the cantilever deflection 4.2. First of all, it is opted to do in-plane and out-of-plane PFM, so the parameters should be chosen twice, once for the horizontal (i.e. in-plane) and once for the vertical (i.e. out-of-plane) case. The parameters are shown in Table 4.1.

Parameters	**Vertical**	**Horizontal**
V_{dc} [V]	1	0
V_{ac} [mV]	3000	3000
ω [kHz]	73	249

Tab. 4.1.: The parameters used for the setup of the PFM measurements.

All the parameters are chosen to optimise the signal-to-noise ratio. To check this, the probe is brought into contact with the sample and the signal is checked. To do PFM, it is crucial to apply an AC component, but a DC component need not be necessary if the signal is already good. The AC component values normally stay within the range of a few voltages [1000 - 4000] mV. In general, the higher these values are taken, the better the signal-to-noise ratio, but this creates more strain on the sample. For the DC component values, during previous measurements, it was found that going beyond 1V can damage the device and thus, a maximum of 1V is taken. The vertical component is driven by the tip, whilst the horizontal component is driven by the sample. Because of the interest in a good signal-to-noise ratio, the frequency is chosen around the contact resonance frequency. [1] Therefore, a search for the contact resonance frequency is done within the software of the Bruker setup. The result is shown in Figure 4.5. As displayed in the figure, a resonance is found at 249kHz. This was then also performed for the vertical component, and a resonance frequency is found at 73kHz. Since wear and tear, or the accumulation of debris can easily influence the resonance frequency, it needs periodically checking and readjusting if necessary. Last but not least, a sweeping of the probe for the scans is done

[1] Note the in-contact part.

under an angle of 90° (i.e. perpendicular to the cantilever). Now everything is set up to perform the actual measurement.

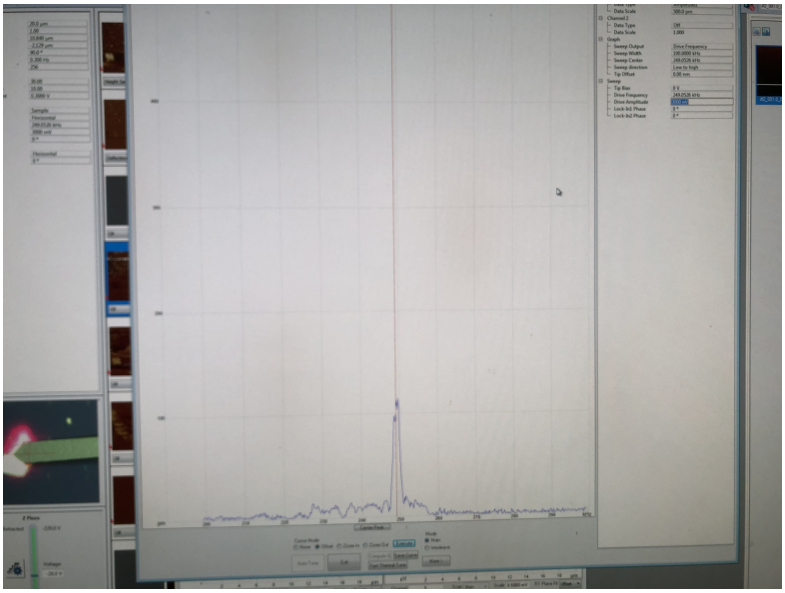

Fig. 4.5.: Image of the found horizontal resonance frequency obtained via the Bruker software. The amplitude of the signal in pm is plotted as a function of the driving frequency in kHz.

4.2.2 Data analysis

First of all, some time is taken to survey the twisted bilayer device in search of rather flat and clean areas. Then a zoom-in is performed on a smaller area and the search for the Moiré pattern. The obtained data are then processed via the open-source software package Gwyddion. All plots shown use the Gwyddion colour map. All the plots undergo a levelling of the plane by subtracting a mean plane. This is then followed by an aligning of the rows using a second-order polynomial. This is to account for unwanted systematic errors and results in more correct height data. The resulting height and deflection error data of the chosen area under investigation are shown in Figure 4.6.

Figure 4 shows a 1x1 μm area. The left plot shows three different height regions. Starting from the top right, a darker and, therefore, lower laying area is shown; this corresponds with the substrate on which the device is fabricated. Movement towards the bottom left corner is accompanied by a discrete jump in height, indicating that the probe is

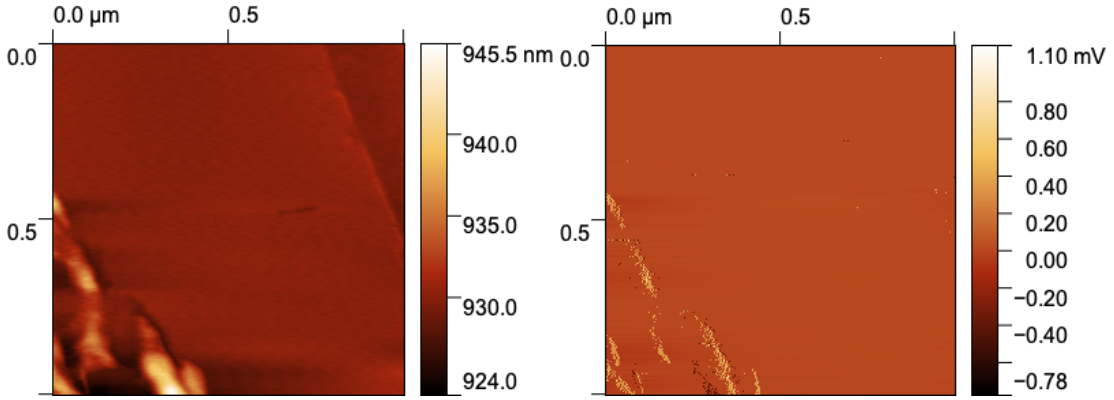

Fig. 4.6.: **Left:** Obtained height data from the measurement. **Right:** Obtained deflection error data from the measurement.

on the device. Moving even further towards the bottom left corner, an uneven region with sudden and gradual increases and decreases in the signal probably correspond with the presents of residues left of the devices. Fabricating devices often include the use of polymers as reported in section 3.4, which can indeed leave residues on the substrate. There is, however, a large, flat and clean area of the device. This is supported by the very low deflection error in this area.

The amplitude and phase obtained from the actual PFM measurement are shown in Figure 4.7 (out-of-plane) and Figure 4.8 (in-plane). Since the piezoelectric response itself holds no relevant information, only whether or not it is present does, so the colorbars hold no information and are thus omitted.

First of all, the phase Figure 4.8, right, clearly shows repetitive lines in the phase signal. The accompanying amplitude also shows these lines at the equivalent position, but they are much less visible than in the phase signal. After these data are taken, a second sweep is performed over the same area, and the lines are visible again at a similar relative position. [2] This indicates that the origin of the signal is indeed coming from the device and not from measurement artefacts. On top of this, the discovered pattern is in line with the expected type of Moiré pattern. However, the lines are quite bendy, and the wavelength of the Moiré pattern is different in different parts of the area. This is probably due to unforeseen strain in the device. Despite the vertical signal not being good, with careful looking, it is possible to identify the same domain walls observed in the vertical phase

[2] the overall area had moved slightly when a second sweep was performed.

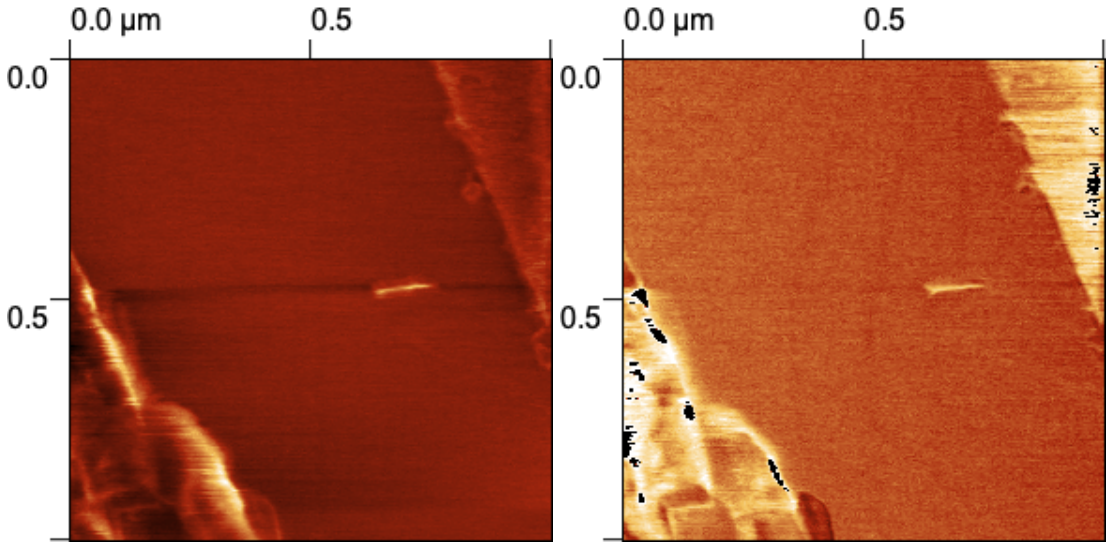

Fig. 4.7.: **Left:** Obtained vertical amplitude data from the measurement. **Right:** Obtained vertical phase data from the measurement.

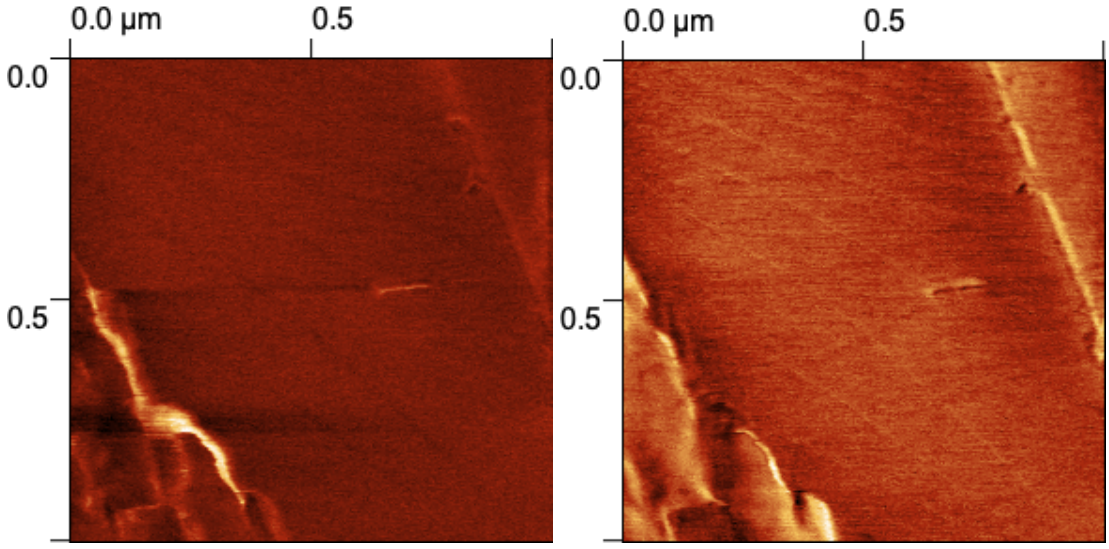

Fig. 4.8.: **Left:** Obtained horizontal amplitude data from the measurement. **Right:** Obtained horizontal phase data from the measurement.

plot as in the horizontal phase. In theory, by combining the data of scans performed at a scan angle of $90°$ and $0°$ it is possible to uncover the whole 6-fold underlying symmetry of the graphene sheets.

The qualitative similarity between Figure 4.2 and the own performed measurements of Figure 4.7, 4.8 indicate the reliability of the performed PFM measurements on graphene and confirms that the device under investigation is indeed twisted.

4.3 Twisted CrSBr

The same analysis performed as in section 4.2 is now applied on the fabricated CrSBr from section 3.5. The thickness of the used flakes is measured during PFM. The results are shown in Figure 4.9

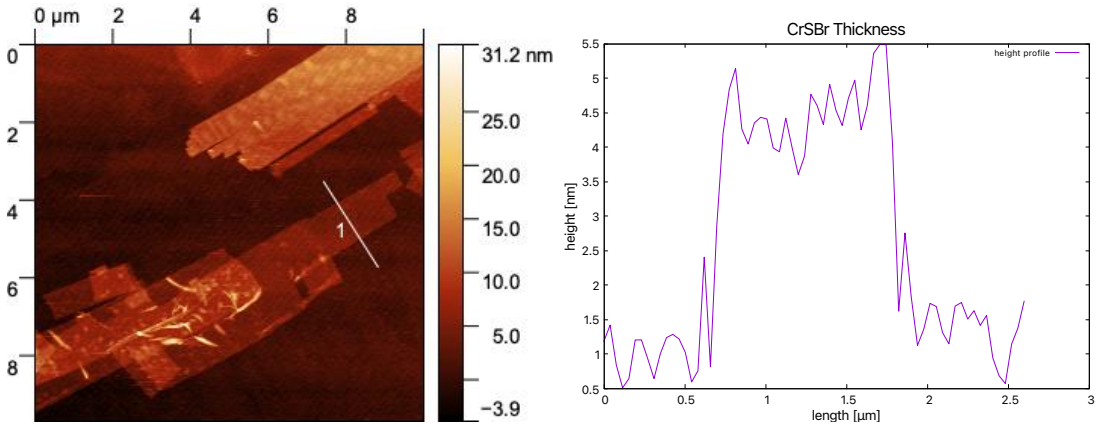

Fig. 4.9.: **Left:** Height data of CrSBr nanostructure. **Right:** Height profile along the line shown in the left image.

The height profile (Figure 4.9, right) indicates a base line around ~ 1.2 nm and a flake thickness of ~ 4.4 nm. Given that a monolayer thickness is ~ 0.8 nm, this corresponds to about 4 layers thick. Same holds for the second transferred flake. The entire nanostructure is hence about 8 layers thick. It also contains some polymer residues as is easily visible from the AFM data image. Now checking the PFM signal shown in Figure 4.10.

Multiple relatively clean zoomed in areas of the nanostructures are evaluated, but no Moiré pattern is found. This is probably due to the fact, that when performing the PFM measurements, the nanostructure needs to be taken out of the glovebox, which then leaves it vulnerable to oxidation. This oxidation layer both interferes with the signal origin of the Moiré pattern and creates an additional barrier which reduce the detecting capabilities of the PFM method.

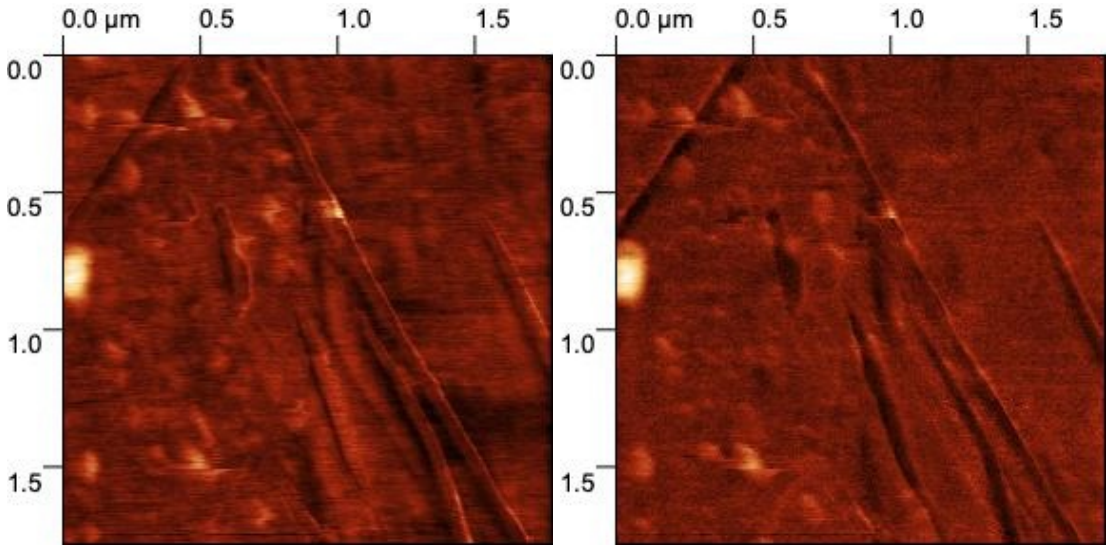

Fig. 4.10.: **Left:** Obtained vertical amplitude data from the measurement. **Right:** Obtained vertical phase data from the measurement.

Conclusion

5

> *The most important thing is that we are all healthy.*
>
> **— Jorden de Bolle**
> (Response to "How did the Quantum 2 exam go?")

This work focuses on 2D materials, which are characterized by having one dimension confined to the nanoscale, resulting in exploitable phenomena not achievable with their traditional three-dimensional counterparts. Particularly, the material CrSBr was investigated, a relatively recently discovered highly promising 2D anti-ferromagnetic semiconductor. This work was the first work to calculate the refractive index of the material ($n_z = 1.4811$) by performing advanced first principle modelling. This new information helped with the fabrication of a twisted CrSBr nanostructure. The PFM measurement technique was then employed to show its feasibility in detecting a Moiré pattern. This was then subsequently applied to the fabricated CrSBr nanostructure. But due to the presence of oxidation layers, it was not possible to detect the Moiré pattern. To overcome this hurdle, the PFM measurements could be done in an inert gas environment.

This work investigated the preliminary, but crucial steps of the fabrication process of CrSBr nanostructures to unlock the novel magnetic properties of the material in the future. For instance, using CrSBr's magnetic properties not standalone, but to enhance an other 2D materials properties seems very promising. This was done very recently in a $MoSe_2$/CrSBr heterostructure. [15] Another interesting heterostructure would be to investigate WSe_2/CrSBr, since spin currents can be induced in WSe_2 using circularly polarised light. [37] In what way the presence of the CrSBr would alter the properties of the spin currents in WSe_2 should be investigated further and might hold intersting new physics.

Bibliography

[1] *ABINIT*. https://www.abinit.org/. accessed 2-April-2023 (cit. on p. 9).

[2] Dan Bing, Yingying Wang, Jing Bai, et al. "Optical contrast for identifying the thickness of two-dimensional materials". In: *Optics Communications* 406 (2018). Optoelectronics and Photonics Based on Two-dimensional Materials, pp. 128–138 (cit. on p. 39).

[3] P. Blake, E. W. Hill, A. H. Castro Neto, et al. "Making graphene visible". In: *Applied Physics Letters* 91.6 (Aug. 2007), p. 063124. eprint: https://pubs.aip.org/aip/apl/article-pdf/doi/10.1063/1.2768624/13197090/063124_1_online.pdf (cit. on p. 39).

[4] Xiangyan Bo, Feng Li, Xinyu Xu, Xiangang Wan, and Yong Pu. "Calculated magnetic exchange interactions in the van der Waals layered magnet CrSBr". In: *New Journal of Physics* 25.1 (Jan. 2023), p. 013026 (cit. on p. 13).

[5] *Bruker setup*. https://anff-q.org.au/event/new-bruker-dimension-icon-xr-afm-webinar/. Performed 6-May-2023 (cit. on p. 49).

[6] Steven J. Byrnes. *Multilayer optical calculations*. 2020. arXiv: 1603.02720 [physics.comp-ph] (cit. on p. 39).

[7] Yuan Cao, Valla Fatemi, Shiang Fang, et al. "Unconventional superconductivity in magic-angle graphene superlattices". In: *Nature* 556.7699 (Apr. 2018), pp. 43–50 (cit. on pp. 6, 7).

[8] I Cheliotis and I Zergioti. "A review on transfer methods of two-dimensional materials". In: *2D Materials* 11.2 (Mar. 2024), p. 022004 (cit. on pp. 35, 37).

[9] Wonbong Choi, Nitin Choudhary, Gang Hee Han, et al. "Recent development of two-dimensional transition metal dichalcogenides and their applications". In: *Materials Today* 20.3 (2017), pp. 116–130 (cit. on pp. 2, 3, 30).

[10] *DFPT with DFT+U*. https://docs.abinit.org/topics/DFPT/. accessed 8-May-2023 (cit. on p. 20).

[11] Anja Förster, Sibylle Gemming, Gotthard Seifert, and David Tománek. "Chemical and Electronic Repair Mechanism of Defects in MoS2 Monolayers". In: *ACS Nano* 11.10 (2017). PMID: 28915006, pp. 9989–9996. eprint: https://doi.org/10.1021/acsnano.7b04162 (cit. on pp. 30, 31).

[12] Riccardo Frisenda, Efrén Navarro-Moratalla, Patricia Gant, et al. "Recent progress in the assembly of nanodevices and van der Waals heterostructures by deterministic placement of 2D materials". In: *Chem. Soc. Rev.* 47 (1 2018), pp. 53–68 (cit. on p. 38).

[13]O. Göser, W. Paul, and H.G. Kahle. “Magnetic properties of CrSBr”. In: *Journal of Magnetism and Magnetic Materials* 92.1 (1990), pp. 129–136 (cit. on p. 3).

[14]Max Heyl and Emil J. W. List-Kratochvil. “Only gold can pull this off: mechanical exfoliations of transition metal dichalcogenides beyond scotch tape”. In: *Applied Physics A* 129.1 (Dec. 2022), p. 16 (cit. on p. 33).

[15]Xinyue Huang, Zhigang Song, Yuchen Gao, et al. *Intrinsic localized excitons in $MoSe_2$/CrSBr heterostructures*. 2024. arXiv: 2405.16079 [cond-mat.mes-hall] (cit. on p. 57).

[16]Yuan Huang, Eli Sutter, Norman N. Shi, et al. “Reliable Exfoliation of Large-Area High-Quality Flakes of Graphene and Other Two-Dimensional Materials”. In: *ACS Nano* 9.11 (2015). PMID: 26336975, pp. 10612–10620. eprint: https://doi.org/10.1021/acsnano.5b04258 (cit. on pp. 31, 41).

[17]Kei Kinoshita, Rai Moriya, Momoko Onodera, et al. “Dry release transfer of graphene and few-layer h-BN by utilizing thermoplasticity of polypropylene carbonate”. In: *npj 2D Materials and Applications* 3.1 (May 2019), p. 22 (cit. on p. 44).

[18]J. Klein, T. Pham, J. D. Thomsen, et al. “Control of structure and spin texture in the van der Waals layered magnet CrSBr”. In: *Nature Communications* 13.1 (Sept. 2022), p. 5420 (cit. on p. 3).

[19]Qiuyang Li, Adam Alfrey, Jiaqi Hu, et al. “Macroscopic transition metal dichalcogenides monolayers with uniformly high optical quality”. In: *Nature Communications* 14.1 (Apr. 2023), p. 1837 (cit. on p. 42).

[20]Siwei Li, Ke Wei, Qirui Liu, Yuxiang Tang, and Tian Jiang. “Twistronics and moiré excitonic physics in van der Waals heterostructures”. In: *Frontiers of Physics* 19.4 (Mar. 2024), p. 42501 (cit. on p. 6).

[21]Kin Fai Mak, Changgu Lee, James Hone, Jie Shan, and Tony F. Heinz. “Atomically Thin MoS_2: A New Direct-Gap Semiconductor”. In: *Phys. Rev. Lett.* 105 (13 Sept. 2010), p. 136805 (cit. on p. 6).

[22]Francisco Marques-Moros, Carla Boix-Constant, Samuel Mañas-Valero, Josep Canet-Ferrer, and Eugenio Coronado. “Interplay between Optical Emission and Magnetism in the van der Waals Magnetic Semiconductor CrSBr in the Two-Dimensional Limit”. In: *ACS Nano* 17.14 (2023). PMID: 37442121, pp. 13224–13231. eprint: https://doi.org/10.1021/acsnano.3c00375 (cit. on p. 5).

[23]Leo J. McGilly, Alexander Kerelsky, Nathan R. Finney, et al. “Visualization of moirésuperlattices”. In: *Nature Nanotechnology* 15.7 (July 1, 2020), pp. 580–584 (cit. on pp. 48, 49).

[24]Roop Kumar Mech, Jean Spièce, Kenji Watanabe, Takashi Taniguchi, and Pascal Gehring. *Versatile polymer method to dry-flip two-dimensional moiré hetero structures for nanoscale surface characterization*. 2024. arXiv: 2406.02819 [cond-mat.mes-hall] (cit. on pp. 43, 44).

[25]*Moiré pattern of 2 Graphene sheets twisted relative to each other*. https://news.softpedia.com/news/Moire-Patterns-Can-Be-Used-to-Analyze-Graphene-140910.shtml. accessed 16-Aug-2024 (cit. on p. 7).

[26]K S Novoselov, A K Geim, S V Morozov, et al. "Electric field effect in atomically thin carbon films". en. In: *Science* 306.5696 (Oct. 2004), pp. 666–669 (cit. on p. 2).

[27]K. S. Novoselov, A. K. Geim, S. V. Morozov, et al. "Electric Field Effect in Atomically Thin Carbon Films". In: *Science* 306.5696 (2004), pp. 666–669. eprint: https://www.science.org/doi/pdf/10.1126/science.1102896 (cit. on p. 31).

[28]Momoko Onodera, Yusai Wakafuji, Taketo Hashimoto, et al. "All-dry flip-over stacking of van der Waals junctions of 2D materials using polyvinyl chloride". In: *Scientific Reports* 12.1 (Dec. 2022), p. 21963 (cit. on p. 43).

[29]Dimitrios G. Papageorgiou, Ian A. Kinloch, and Robert J. Young. "Mechanical properties of graphene and graphene-based nanocomposites". In: *Progress in Materials Science* 90 (2017), pp. 75–127 (cit. on p. 2).

[30]*PFM practice*. https://www.attocube.com/en/products/microscopes/fundamentals/piezoresponse-force-microscopy. Performed 20-July-2024 (cit. on p. 47).

[31]*PFM theory*. http://3.101.126.204/jp/park-spm-modes/93-dielectric-piezoelectric/230-piezoelectric-force-microscopy-pfm. Performed 20-July-2024 (cit. on p. 47).

[32]S. V. Satya Prasad, Raghvendra Kumar Mishra, Swati Gupta, S. B. Prasad, and Subhash Singh. "Introduction, History, and Origin of Two Dimensional (2D) Materials". In: *Advanced Applications of 2D Nanostructures: Emerging Research and Opportunities*. Ed. by Subhash Singh, Kartikey Verma, and Chander Prakash. Singapore: Springer Singapore, 2021, pp. 1–9 (cit. on p. 2).

[33]*probe specs*. https://www.nanosensors.com/pointprobe-plus-contact-mode-ptir5-coating-afm-tip-PPP-CONTPt (cit. on p. 49).

[34]*Pseuopotential NC, LDA from pseudo-dojo*. http://www.pseudo-dojo.org. accessed 8-May-2023 (cit. on pp. 11, 25).

[35]*Pseuopotential PAW, LDA from pseudo-dojo*. http://www.pseudo-dojo.org. accessed 8-May-2023 (cit. on p. 20).

[36]*Pseuopotential PAW, PBE from pseudo-dojo*. http://www.pseudo-dojo.org. accessed 22-April-2023 (cit. on p. 11).

[37]Cedric Robert, Sangjun Park, Fabian Cadiz, et al. "Spin/valley pumping of resident electrons in WSe2 and WS2 monolayers". In: *Nature Communications* 12.1 (Sept. 2021), p. 5455 (cit. on p. 57).

[38]Mingyu Sang, Jongwoon Shin, Kiho Kim, and Ki Jun Yu. "Electronic and Thermal Properties of Graphene and Recent Advances in Graphene Based Electronics Applications". In: *Nanomaterials* 9.3 (2019) (cit. on p. 2).

[39] Evan J Telford, Avalon H Dismukes, Kihong Lee, et al. “Layered antiferromagnetism induces large negative magnetoresistance in the van der Waals semiconductor CrSBr”. en. In: *Adv. Mater.* 32.37 (Sept. 2020), e2003240 (cit. on p. 17).

[40] Evan J. Telford, Avalon H. Dismukes, Kihong Lee, et al. “Layered Antiferromagnetism Induces Large Negative Magnetoresistance in the van der Waals Semiconductor CrSBr”. In: *Advanced Materials* 32.37 (Aug. 2020), p. 2003240 (cit. on p. 4).

[41] Evan J. Telford, Avalon H. Dismukes, Kihong Lee, et al. “Layered Antiferromagnetism Induces Large Negative Magnetoresistance in the van der Waals Semiconductor CrSBr”. In: *Advanced Materials* 32.37 (2020), p. 2003240. eprint: `https://onlinelibrary.wiley.com/doi/pdf/10.1002/adma.202003240` (cit. on pp. 4, 9).

[42] Matěj Velický, Gavin E. Donnelly, William R. Hendren, et al. “Mechanism of Gold-Assisted Exfoliation of Centimeter-Sized Transition-Metal Dichalcogenide Monolayers”. In: *ACS Nano* 12.10 (2018). PMID: 30265515, pp. 10463–10472. eprint: `https://doi.org/10.1021/acsnano.8b06101` (cit. on p. 32).

[43] Yusai Wakafuji, Momoko Onodera, Satoru Masubuchi, et al. “Evaluation of polyvinyl chloride adhesion to 2D crystal flakes”. In: *npj 2D Materials and Applications* 6.1 (June 2022), p. 44 (cit. on pp. 43, 44).

[44] Adam J Watson, Wenbo Lu, Marcos H D Guimarães, and Meike Stöhr. “Transfer of large-scale two-dimensional semiconductors: challenges and developments”. In: *2D Materials* 8.3 (May 2021), p. 032001 (cit. on p. 34).

[45] Nathan P. Wilson, Kihong Lee, John Cenker, et al. “Interlayer electronic coupling on demand in a 2D magnetic semiconductor”. In: *Nature Materials* 20.12 (Dec. 2021), pp. 1657–1662 (cit. on p. 13).

[46] Ke Yang, Guangyu Wang, Lu Liu, Di Lu, and Hua Wu. “Triaxial magnetic anisotropy in the two-dimensional ferromagnetic semiconductor CrSBr”. In: *Phys. Rev. B* 104 (14 Oct. 2021), p. 144416 (cit. on pp. 10, 13, 18, 19).

List of Figures

List of Tables

Appendix

A

A.1 Convergence study: U=6, J=0.8

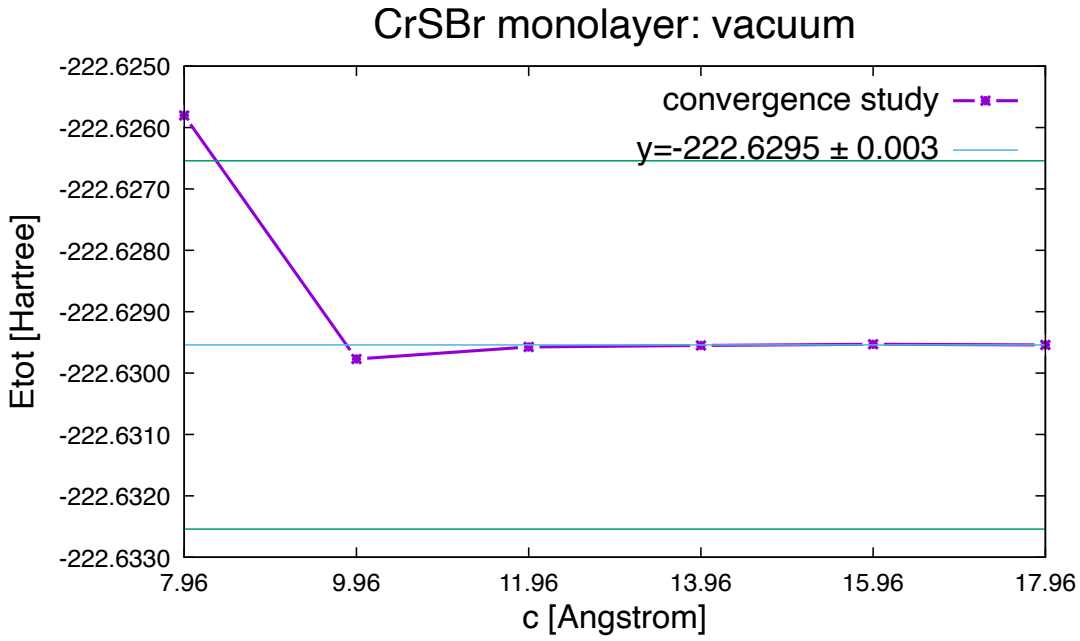

Fig. A.1.: Convergence study of total energy with respect to the c-axis for monolayer CrSBr in DFT+U, $U = 6$ eV and $J = 0.8$ eV. Obtained value c $= 9.96$ Å.

Vacuum

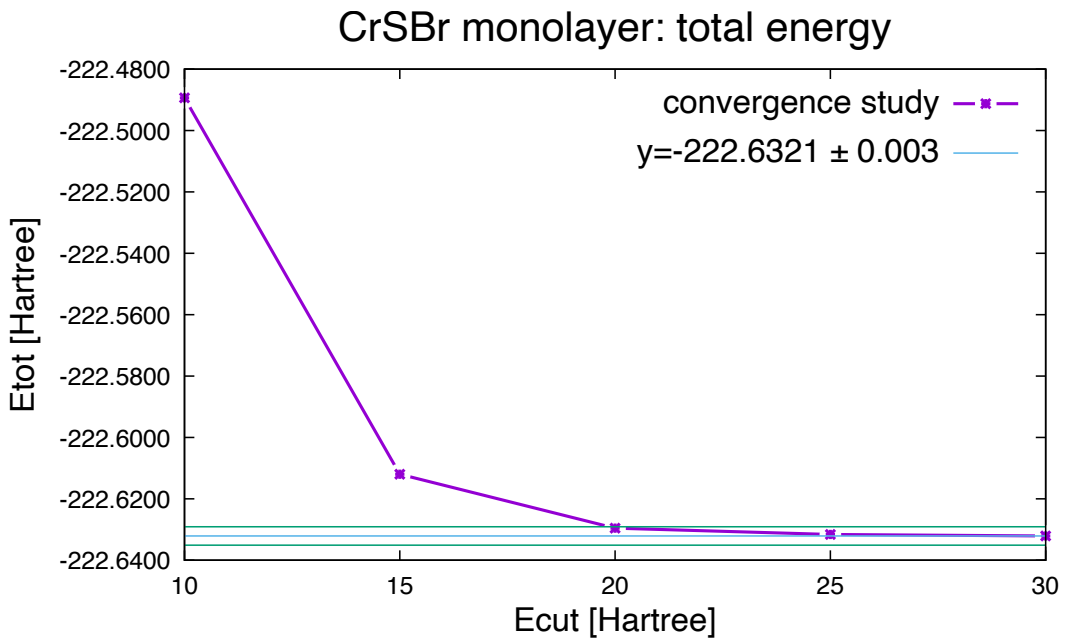

Fig. A.2.: Convergence study of total energy with respect to ecut for monolayer CrSBr in DFT+U, $U = 6$ eV and $J = 0.8$ eV. Obtained value ecut $= 20$.

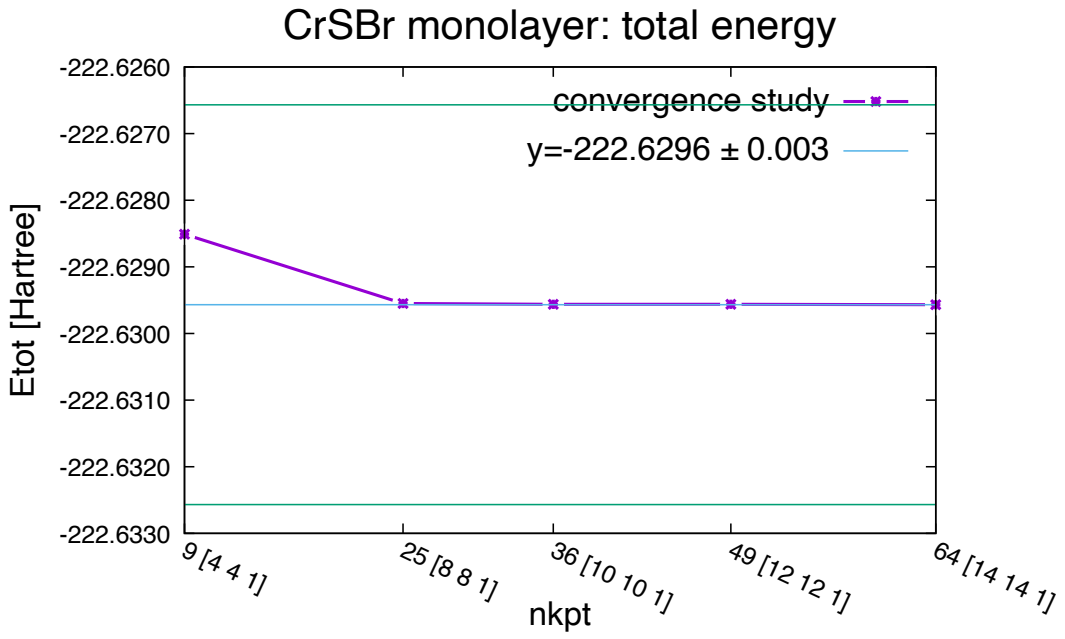

Fig. A.3.: Convergence study of total energy with respect to kpoints for monolayer CrSBr in DFT+U, $U = 6$ eV and $J = 0.8$ eV. Obtained value kpoints $= [4\ 4\ 1]$.

Total energy

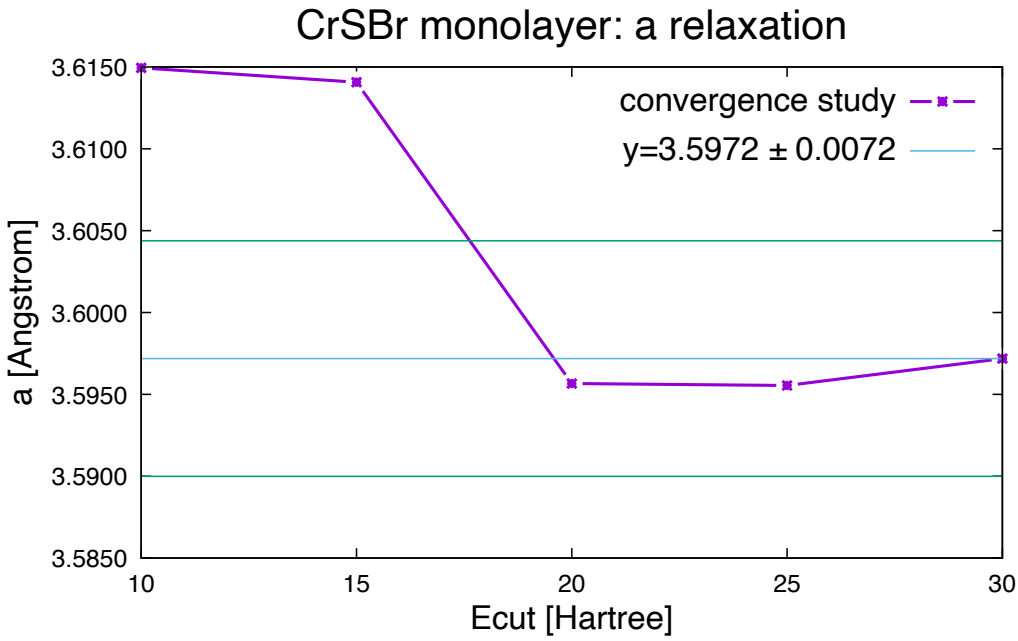

Fig. A.4.: Convergence study of a-axis with respect to ecut for monolayer CrSBr in DFT+U, $U = 6$ eV and $J = 0.8$ eV. Obtained value ecut $= 20$.

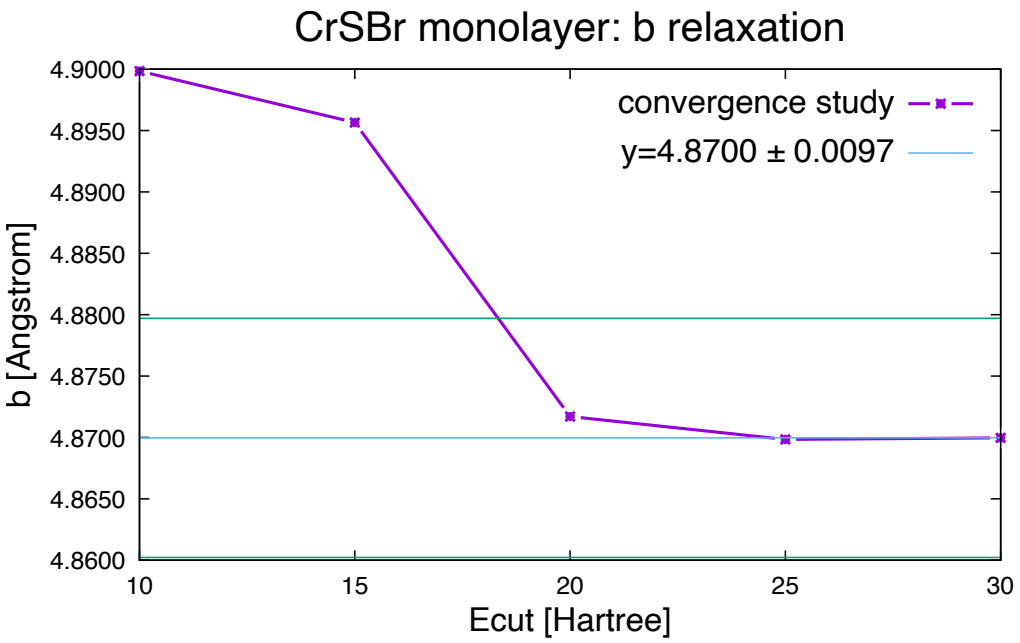

Fig. A.5.: Convergence study of b-axis with respect to ecut for monolayer CrSBr in DFT+U, $U = 6$ eV and $J = 0.8$ eV. Obtained value ecut $= 20$.

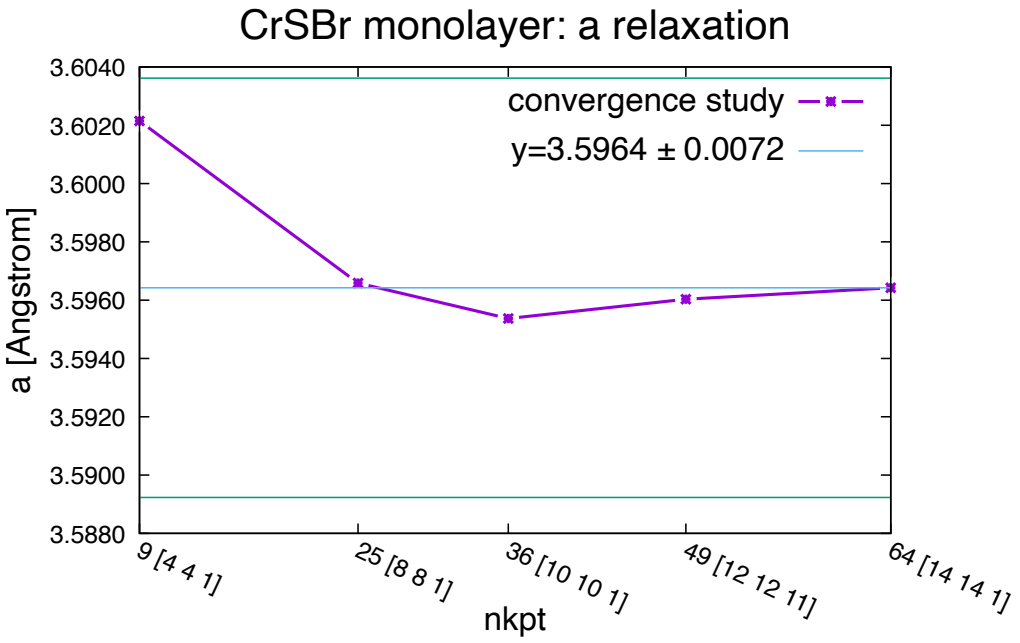

Fig. A.6.: Convergence study of a-axis with respect to kpoints for monolayer CrSBr in DFT+U, $U = 6$ eV and $J = 0.8$ eV. Obtained value kpoints $= [4\ 4\ 1]$.

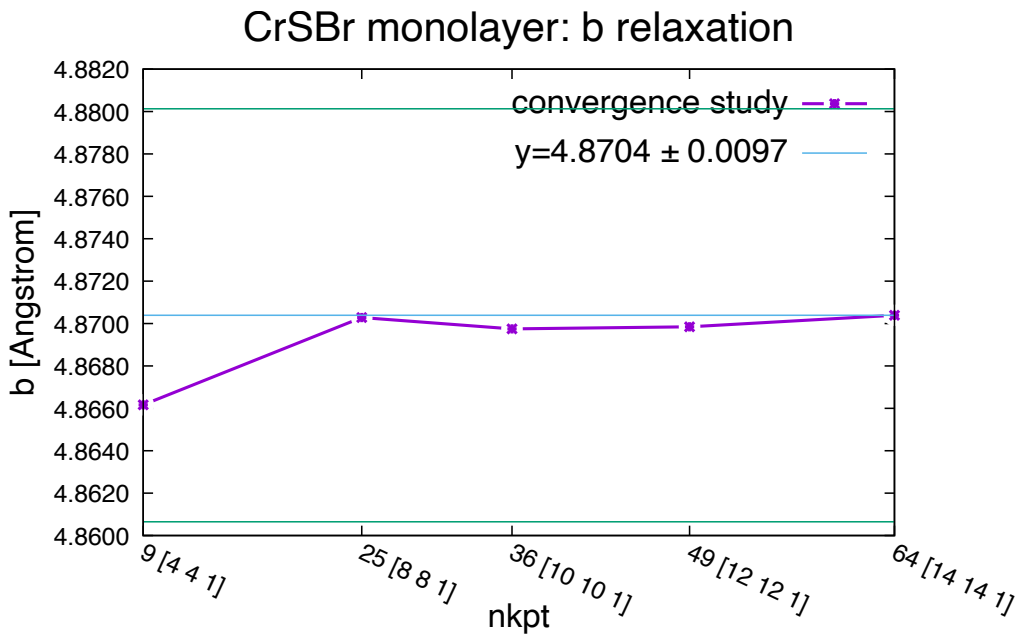

Fig. A.7.: Convergence study of b-axis with respect to kpoints for monolayer CrSBr in DFT+U, $U = 6$ eV and $J = 0.8$ eV. Obtained value kpoints $= [4\ 4\ 1]$.

Relaxation

A.2 Convergence study: refractive index NC

Ecut The convergence studies of n_x, n_y and n_z with respect to ecut are shown in Figure A.8, Figure A.9 and Figure A.10, respectively.

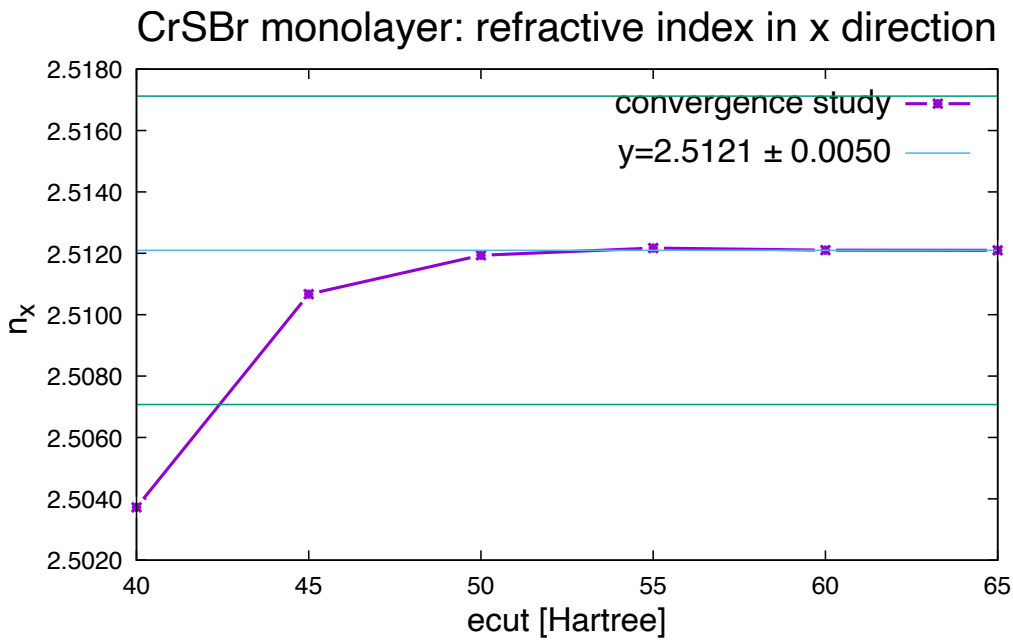

Fig. A.8.: Convergence study of n_x with respect to ecut for monolayer CrSBr in DFT + scissor cut. Obtained value ecut $= 45$.

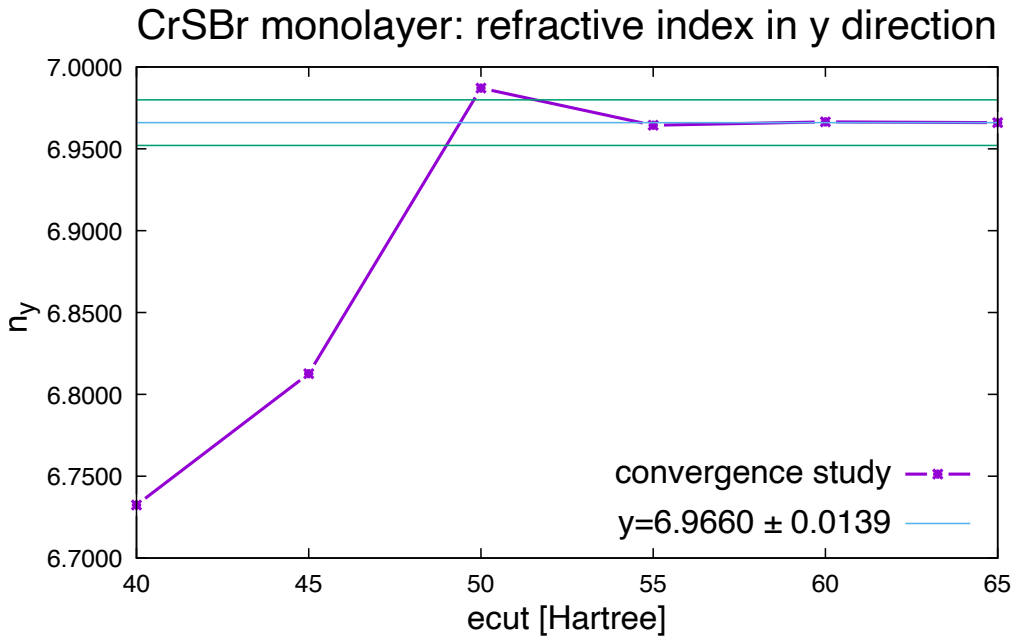

Fig. A.9.: Convergence study of n_y with respect to ecut for monolayer CrSBr in DFT + scissor cut. Obtained value ecut $= 55$.

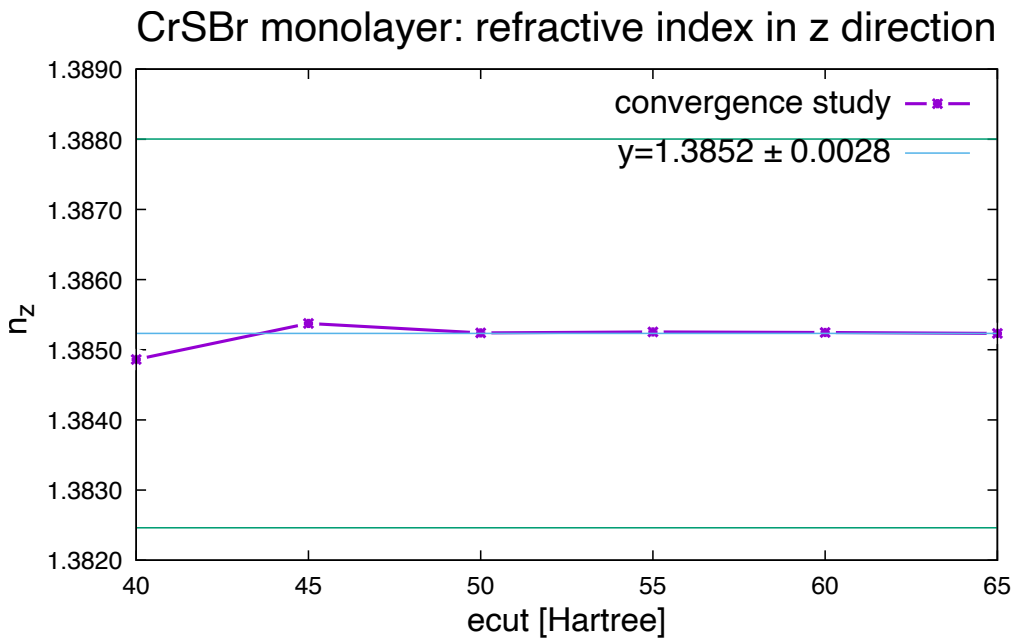

Fig. A.10.: Convergence study of n_z with respect to ecut for monolayer CrSBr in DFT + scissor cut. Obtained value ecut $= 40$.

Kpoints Now with ecut $= 55$, the convergence studies of n_x, n_y and n_z with respect to kpoints are shown in Figure A.11, Figure A.12 and Figure A.13, respectively.

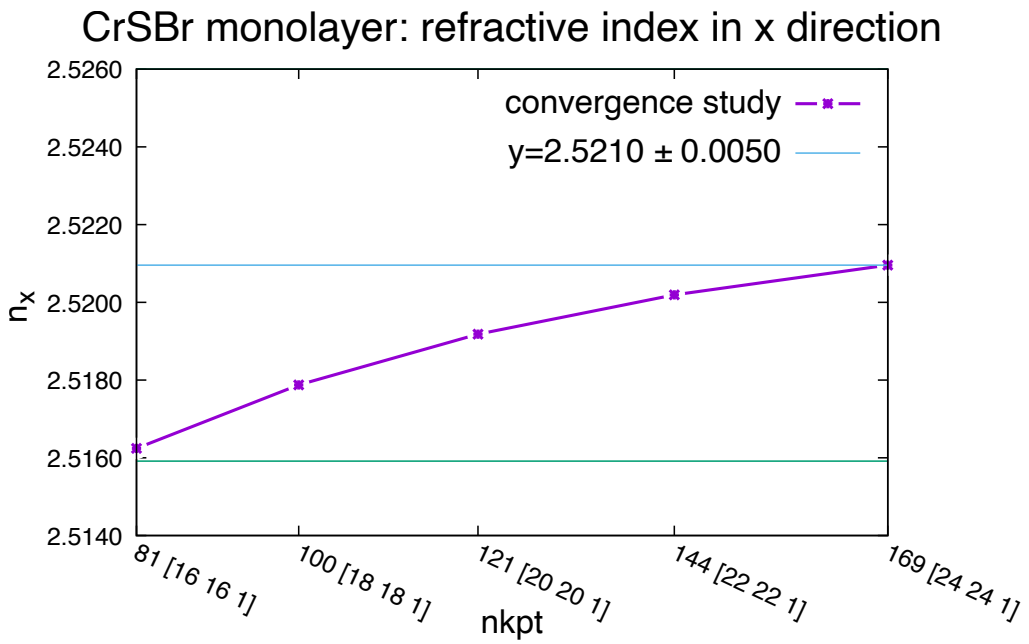

Fig. A.11.: Convergence study of n_x with respect to kpoints for monolayer CrSBr in DFT + scissor cut. Obtained value kpoints = [16 16 1].

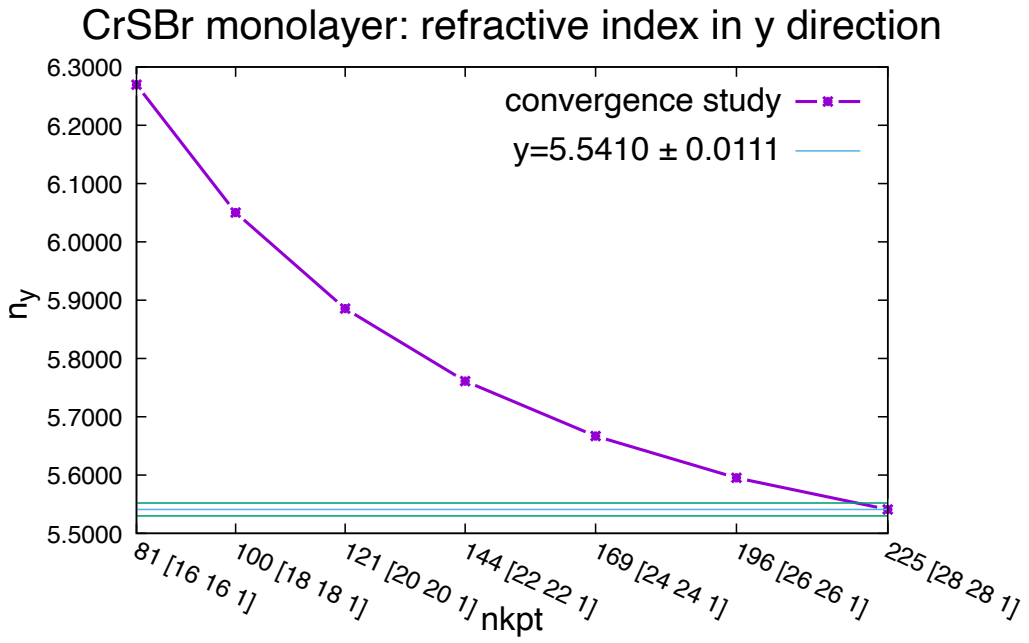

Fig. A.12.: Convergence study of n_y with respect to kpoints for monolayer CrSBr in DFT + scissor cut. Obtained value kpoints = [28 28 1].

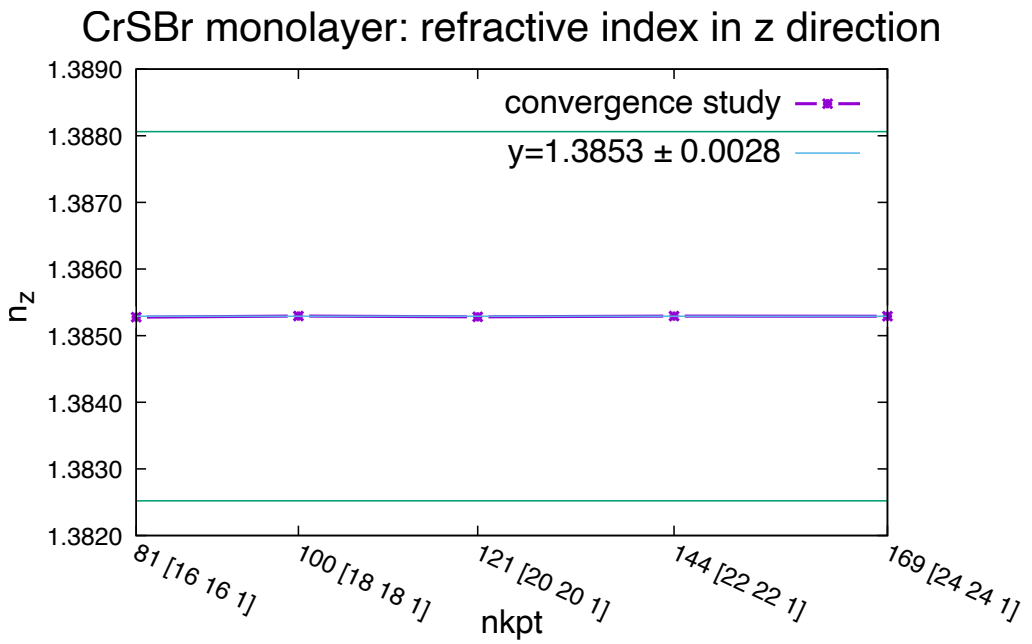

Fig. A.13.: Convergence study of n_z with respect to kpoints for monolayer CrSBr in DFT + scissor cut. Obtained value kpoints = [16 16 1].

Vacuum Now with kpoints = [20 20 1] (see section 2.2.2), the convergence studies of n_x, n_y and n_z with respect to c are shown in Figure A.14, Figure A.15 and Figure A.16, respectively.

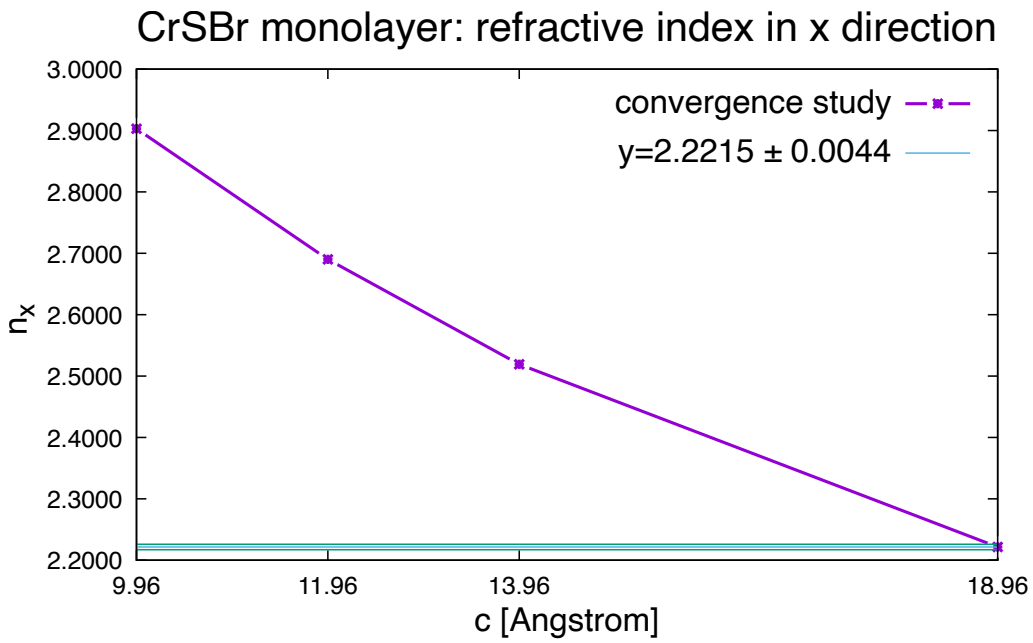

Fig. A.14.: Convergence study of n_x with respect to c for monolayer CrSBr in DFT + scissor cut. Obtained value $c = 18.96$ Å.

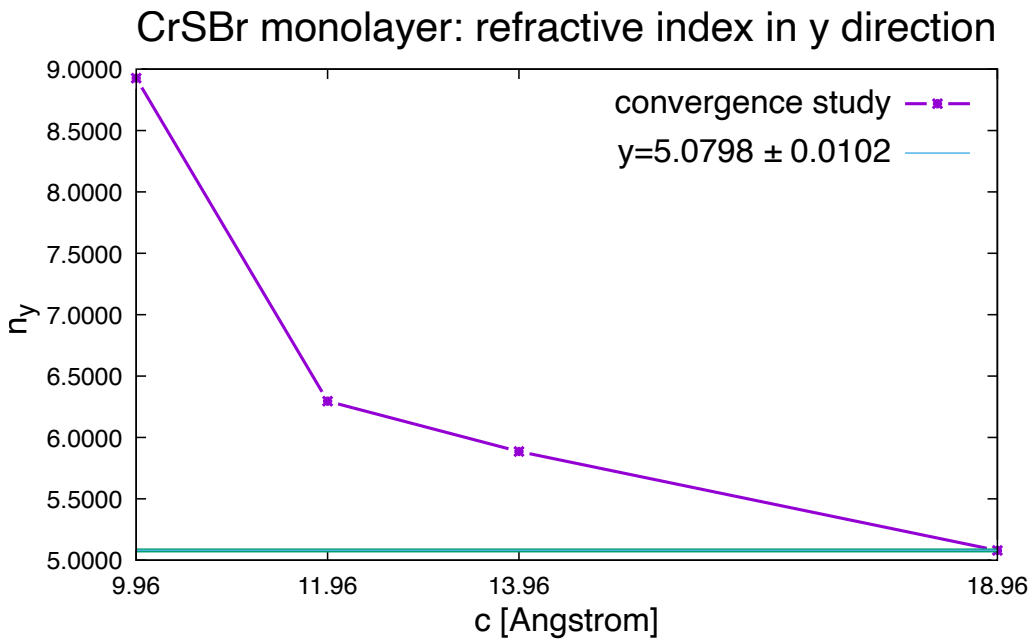

Fig. A.15.: Convergence study of n_y with respect to c for monolayer CrSBr in DFT + scissor cut. Obtained value $c = 18.96$ Å.

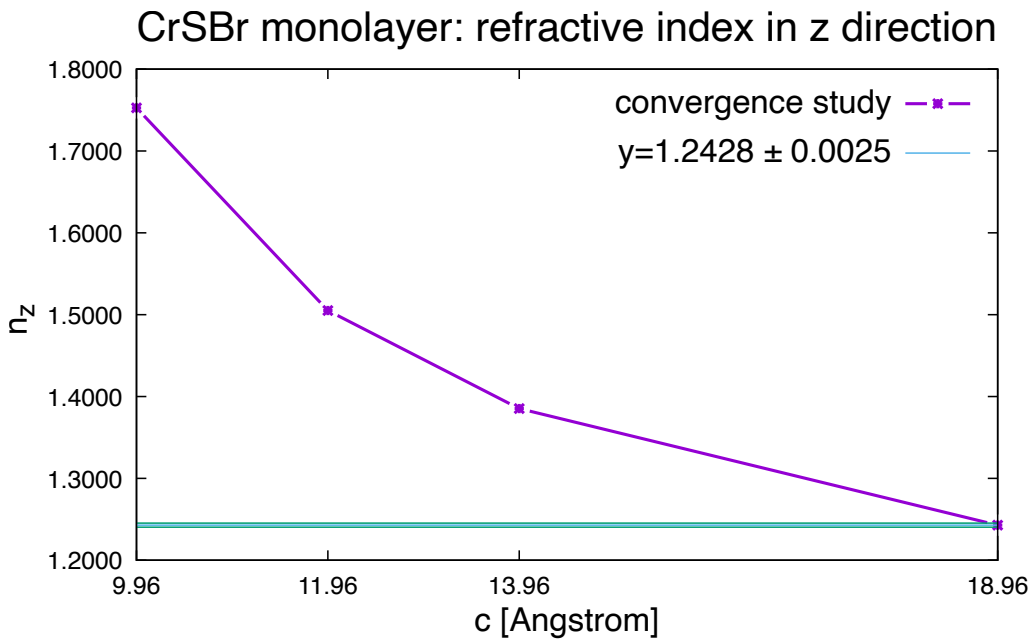

Fig. A.16.: Convergence study of n_z with respect to c for monolayer CrSBr in DFT + scissor cut. Obtained value $c = 18.96$ Å.

A.3 Impact of sciss cut: input files

Highlighted in red is what changed between the 2 inputs.

```
# CrSBr setup
ndtset  3

#Ground state calculation
kptopt1   1        # Automatic generation of k points, taking
                   # into account the symmetry
tolvrs1   1.0d-18  # SCF stopping criterion
nbdbuf1   10
nband1    50

occ1     1.000000  1.000000  1.000000  1.000000  1.000000  1.000000
         1.000000  1.000000  1.000000  1.000000  1.000000  1.000000
```

```
          1.000000  1.000000  1.000000  1.000000  1.000000  1.000000
          1.000000  1.000000  1.000000  1.000000  1.000000  1.000000
          1.000000  1.000000  1.000000  1.000000  1.000000  1.000000
          1.000000  1.000000  1.000000  1.000000  1.000000  1.000000
          1.000000  1.000000  1.000000  1.000000  0.000000  0.000000
          0.000000  0.000000  0.000000  0.000000  0.000000  0.000000
          0.000000  0.000000
          1.000000  1.000000  1.000000  1.000000  1.000000  1.000000
          1.000000  1.000000  1.000000  1.000000  1.000000  1.000000
          1.000000  1.000000  1.000000  1.000000  1.000000  1.000000
          1.000000  1.000000  1.000000  1.000000  1.000000  1.000000
          1.000000  1.000000  1.000000  1.000000  1.000000  1.000000
          1.000000  1.000000  1.000000  1.000000  0.000000  0.000000
          0.000000  0.000000  0.000000  0.000000  0.000000  0.000000
          0.000000  0.000000  0.000000  0.000000  0.000000  0.000000
          0.000000  0.000000

#Response Function calculation : d/dk
rfelfd2   2        # Activate the calculation of the d/dk perturbation
rfdir2   1 1 1     # Pertubation in all directions

nbdbuf2   10
nband2    50

occ2      1.000000  1.000000  1.000000  1.000000  1.000000  1.000000
          1.000000  1.000000  1.000000  1.000000  1.000000  1.000000
          1.000000  1.000000  1.000000  1.000000  1.000000  1.000000
          1.000000  1.000000  1.000000  1.000000  1.000000  1.000000
          1.000000  1.000000  1.000000  1.000000  1.000000  1.000000
          1.000000  1.000000  1.000000  1.000000  1.000000  1.000000
          1.000000  1.000000  1.000000  1.000000  0.000000  0.000000
          0.000000  0.000000  0.000000  0.000000  0.000000  0.000000
          0.000000  0.000000
          1.000000  1.000000  1.000000  1.000000  1.000000  1.000000
          1.000000  1.000000  1.000000  1.000000  1.000000  1.000000
          1.000000  1.000000  1.000000  1.000000  1.000000  1.000000
```

```
          1.000000  1.000000  1.000000  1.000000  1.000000  1.000000
          1.000000  1.000000  1.000000  1.000000  1.000000  1.000000
          1.000000  1.000000  1.000000  1.000000  0.000000  0.000000
          0.000000  0.000000  0.000000  0.000000  0.000000  0.000000
          0.000000  0.000000  0.000000  0.000000  0.000000  0.000000
          0.000000  0.000000

nqpt2   1
qpt2   0.0 0.0 0.0 # This is a calculation at the Gamma point

getwfk2   -1       # Uses as input the output wf of the previous dataset

kptopt2   2        # Automatic generation of k points,
                   # using only the time-reversal symmetry to decrease
                   # the size of the k point set.

iscf2  -3          # The d/dk perturbation must be treated
                   # in a non-self-consistent way
tolwfr2   1.0d-18  # Must use tolwfr for non-self-consistent calculations
                   # Here, the value of tolwfr is very low.

#Response Function calculation : electric field perturbation and phonons
rfelfd3   3        # Activate the calculation of the electric field perturbation
rfdir3   1 1 1     # All directions are selected.

dfpt_sciss3 1.13 eV

nbdbuf3   10
nband3    50

occ3     1.000000  1.000000  1.000000  1.000000  1.000000  1.000000
         1.000000  1.000000  1.000000  1.000000  1.000000  1.000000
         1.000000  1.000000  1.000000  1.000000  1.000000  1.000000
         1.000000  1.000000  1.000000  1.000000  1.000000  1.000000
         1.000000  1.000000  1.000000  1.000000  1.000000  1.000000
         1.000000  1.000000  1.000000  1.000000  1.000000  1.000000
```

```
          1.000000  1.000000  1.000000  1.000000  0.000000  0.000000
          0.000000  0.000000  0.000000  0.000000  0.000000  0.000000
          0.000000  0.000000
          1.000000  1.000000  1.000000  1.000000  1.000000  1.000000
          1.000000  1.000000  1.000000  1.000000  1.000000  1.000000
          1.000000  1.000000  1.000000  1.000000  1.000000  1.000000
          1.000000  1.000000  1.000000  1.000000  1.000000  1.000000
          1.000000  1.000000  1.000000  1.000000  1.000000  1.000000
          1.000000  1.000000  1.000000  1.000000  0.000000  0.000000
          0.000000  0.000000  0.000000  0.000000  0.000000  0.000000
          0.000000  0.000000  0.000000  0.000000  0.000000  0.000000
          0.000000  0.000000

getwfk3   -2       # Uses as input wfs the output wfs of the dataset 1
getddk3   -1       # Uses as input ddk wfs the output of the dataset 2

kptopt3   2        # Automatic generation of k points,
                   # using only the time-reversal symmetry to decrease
                   # the size of the k point set.
tolvrs3   1.0d-18

##The same for all sets
#Definition of the unit cell
acell 6.79477881000444 9.20613966114326 15.042140670471296

rprim  1 0 0
       0 1 0
       0 0 1.75376884 #13.96 Angstrom

#Definition of the atom types
ntypat 3           # There is only one type of atom
znucl 24 16 35

pp_dirpath "/globalscratch/ucl/pamo/lsmet/Project/potentials/norm_conserving/"        # This
                                 # pseudopotentials for tests are stored
pseudos "Cr.psp8, S.psp8, Br.psp8"
```

```
                                    # Name and location of the pseudopotential

#Definition of the atoms
natom 6
typat 1 1 2 2 3 3

xcart

3.39738940494771E+00  2.55521705E-15  2.994846561
-1.84821137E-15  4.60306983066153E+00  6.897817535
3.39738940494771E+00  4.6030698306616E+00 3.774454408
-1.84821137E-15  2.55521705E-15  6.118209688
-1.84821137E-15  2.55521705E-15 -0.4317282071
3.39738940494771E+00  4.60306983066153E+00  10.3243923

chksymtnons 2 #to overrule warning of FFT grid

ecut 55

#spin polarised (FM)
nsppol 2
spinat   0.0 0.0 3.0
         0.0 0.0 3.0
         0.0 0.0 0.0
         0.0 0.0 0.0
         0.0 0.0 0.0
         0.0 0.0 0.0

occopt 0

#Definition of the k-point grid

ngkpt 12 12 1
nshiftk 1
shiftk 0.0 0.0 0.0
```

```
#Definition of the SCF procedure
nstep 200          # Maximal number of SCF cycles
diemac 12.0
AUTOPARAL 1        #to make better use of the cpus
```

UNIVERSITÉ CATHOLIQUE DE LOUVAIN
École polytechnique de Louvain
Rue Archimède, 1 bte L6.11.01, 1348 Louvain-la-Neuve, Belgique | **www.uclouvain.be/epl**